A Family of Finite-Volume Methods for Computing Pressure Gradient Force in an Ocean Model with a Topography-Following Vertical Coordinate

Alexander F. Shchepetkin
and
James C. McWilliams

Institute of Geophysics and Planetary Physics,
University of California at Los Angeles,
405 Hilgard Avenue, Los Angeles, CA 90024-1567

e-mail: *alex@atmos.ucla.edu* *jcm@atmos.ucla.edu*

March, 2001

Abstract. Discretization of the pressure gradient force is a long-standing problem in σ-coordinate ocean modeling. As long as the isosurfaces of vertical coordinate are not aligned with either geopotential surfaces or isopycnals, the horizontal pressure gradient consists of two large terms that tend to cancel each other. The associated pressure gradient error stems from interference of the discretization errors of these terms. The situation is further complicated by the non-orthogonality of the terrain-following coordinate system and by the common practice of using highly non-uniform stretching for the vertical grids, which, unless special precautions are made, causes both loss of accuracy of vertical discretization, and increase in interference in the error of the pressure gradient force.

In this manuscript we design pressure gradient schemes which insure more accurate balance of terms and which also do not suffer as much loss of accuracy with non-uniform vertical grids at relatively coarse resolution. These schemes are based on local, conservative, limited-oscillation vertical spline reconstruction of the density field with subsequent projection of the spline-based derivatives of density onto isosurfaces of vertical coordinate in order to compensate the hydrostatic errors associated with the non-orthogonality of the vertical grid.

discretized in a manner similar to that described above, except that now vertical integration becomes the second step rather than the first and field P never appears explicitly in the model. Because of form of (1.7), these methods are often referred as *density-Jacobian*, opposite to the *pressure-Jacobian* methods described above. The pressure gradient schemes in two commonly used terrain-following ocean models (POM, SCRUM) belong to this class.

Song, 1998 and Song & Wright, 1998 argue that a density-Jacobian method is inherently more accurate than a pressure-Jacobian. Indeed, it is easy to see that if the basic second-order techniques (2-point differencing, interpolation and trapezoidal integration) are used and if the density field is a linear function of z, then the error of a density-Jacobian method vanishes identically. On the other hand, a linear density profile corresponds to quadratic pressure; therefore discretizations based on a linear fit for the pressure field are not able to capture it correctly resulting in hydrostatic error. Therefore, with a standard numerical implementation, density-Jacobian methods tend to be one order of accuracy better than pressure-Jacobian.

On the other hand, Lin, 1997 points out that it is advantageous to discretize pressure gradient force using a finite-volume technique. An attractive feature of this approach is that the discretized pressure gradient term naturally appears in flux-divergent form, which makes the proof of momentum and bottom torque consistency [cf. Arakawa & Suarez, 1983; Song & Wright, 1998] virtually trivial. There is no obvious way to cast adensity-Jacobian scheme into the form of a difference of pressure fluxes.

Similarly to most other pressure-Jacobian methods, Lin's method uses a linear assumption about the spatial structure of the pressure field, thus failing to produce zero error in the case of linear density field. This conflict between accuracy and conservation properties of σ-coordinate pressure gradient schemes is not uncommon (e.g. Beckmann & Haidvogel, 1993; Song & Wright, 1998)

It is also not surprizing that ocean models tend to use density-Jacobian, while atmospheric models use pressure-Jacobian. In comparison with the atmosphere, the ocean is typically more strongly stratified and the stratification is much more spatially variable: it is not unusual to see a change of Brunt-Väisäla frequency by two orders of magnitude throughout a vertical column. Much of the vertical density gradient in atmospheric models is due to the compressibility effect, which may be absorbed by special mapping techniques as well as by choice of vertical coordinate system (pressure instead of geopotential; Arakawa & Suarez, 1983). No such procedures are possible in ocean models, which makes the accuracy of representation of vertical profiles of density and pressure a higher priority in ocean modeling.

Atmospheric models are more cautious about energetic consistency of discretized tracer and momentum equations. Since in stratified media the density profile and pressure field are redistributed predominantly by vertical velocity [1], and since vertical velocity is obtained from divergence of horizontal velocity, which in turn is controlled by the horizontal pressure gradient, failure to obtain cancellation of potential and kinetic energy conversion terms (the so-called "omega-alpha" terms) for the discretized tracer and momentum equations may cause computational instability (Janjic, 1977; Arakawa & Suarez, 1983). As the result, pressure gradient schemes in atmospheric models are designed in concent with advection schemes for tracers. Pressure-Jacobian schemes facilitate analytic proof of energetic consistency. The desire for energetic consistency may impede the search for higher than second-order accurate pressure gradient schemes because analytic proof becomes too difficult.

The high-order pressure gradient schemes available to date follow the path of straightforward discretization of (1.6) using a spectral method in the vertical direction in combination with either conventional or compact forth-order finite differences and interpolations in horizontal (McCalpin, 1994); or spectral in combination with compact differencing up to the sixth order of accuracy (Chu & Fan, 1997; Chu & Fan, 1998). This was shown to be reasonably successful for few test problems, but practically useless for real-world simulations. The approach relies exclusively on the smallness of the truncation errors of the elementary discretizations (computation of the first derivative and mid-point interpolation), which is justifiable only when the density field is smooth on the grid scale.

In the present study we seek a high-order accuracy extension to Lin's method that retains its conservation properties, yet provides faster convergence rate than the existent pressure-Jacobian and even density-Jacobian schemes. All algorithms designed here have zero hydro-

[1] In the case of linearized momentum equations, the only mechanism of changing density distribution is due to interaction of background statification and vertical velocity. This is believed to be the dominant mechanism in the general case too.

simple trapezoidal rule to evaluate the integrals in (2.4),

$$FX_{i,k} = \frac{P_{i,k+\frac{1}{2}} + P_{i,k-\frac{1}{2}}}{2} (z_{i,k+\frac{1}{2}} - z_{i,k-\frac{1}{2}}) \tag{2.6}$$

$$FC_{i+\frac{1}{2},k+\frac{1}{2}} = \frac{P_{i+1,k+\frac{1}{2}} + P_{i,k+\frac{1}{2}}}{2} (z_{i+1,k+\frac{1}{2}} - z_{i,k+\frac{1}{2}}) \,. \tag{2.7}$$

When ρ is a linear function of depth, P changes quadratically with depth. However, Lin's method makes a piecewise-linear approximation for P, which results in residual error for pressure gradient force, as illustrated in Fig. 2. Shown on the left is the grid element around $u_{i+\frac{1}{2},k}$ (the same as in Fig. 1). It is assumed that exact values of P are known at its four corners. Parabolic segment on the right shows the exact distribution of pressure, while straight lines represent the distribution as it is interpreted by the trapezoidal integration formulas. Solid lines represent fluxes with positive sign in (2.3), while dashed lines correspond to fluxes with negative sign. The erroneous pressure gradient is equal to the difference between the light shaded and dark shaded areas.

3. Pressure Gradient Algorithms

The most straightforward way to reduce erroneous pressure gradient of Lin's method problem is to replace trapezoidal integrations in (2.4) with more accurate ones, using cubic and quintic polynomial fits,

$$\int_{\xi_-}^{\xi_+} f(\xi)\, d\xi \approx \Delta\xi \cdot \frac{f_+ + f_-}{2} - \Delta\xi^2 \cdot \frac{f'_+ - f'_-}{12} \tag{3.1}$$

$$\int_{\xi_-}^{\xi_+} f(\xi)\, d\xi \approx \Delta\xi \cdot \frac{f_+ + f_-}{2} - \Delta\xi^2 \cdot \frac{f'_+ - f'_-}{10} + +\Delta\xi^3 \cdot \frac{f''_+ + f''_-}{120} \tag{3.2}$$

where $\Delta\xi \equiv \xi_+ - \xi_-$, $f_\pm \equiv f(\xi_\pm)$ are the values of function at the ends of the interval of integration, and

$$f'_\pm \equiv \left.\frac{\partial f}{\partial \xi}\right|_{\xi=\xi_\pm} \quad \text{and} \quad f''_\pm \equiv \left.\frac{\partial^2 f}{\partial \xi^2}\right|_{\xi=\xi_\pm} \tag{3.3}$$

are the side values of first and second derivatives. Eqs. (3.1) and (3.2) are exact for polynomials of powers up to 3 and 5, while beyond that their leading-order truncation errors are estimated as

$$-\frac{1}{30} \cdot \frac{1}{4!} \cdot \frac{\partial^4 f}{\partial \xi^4} \Delta\xi^5 \quad \text{and} \quad +\frac{1}{140} \cdot \frac{1}{6!} \cdot \frac{\partial^6 f}{\partial \xi^6} \Delta\xi^7 \,, \tag{3.4}$$

provided that the side values and derivatives are known exactly. This indicates fourth and sixth orders of accuracy, respectively, one order less than in (3.4), because the integral itself is proportional to $\Delta\xi$.

In order to apply (3.1) or (3.2) one needs to know derivatives of P. One approach is to construct a polynomial fit for P using extra additional grid points, see Appendix A. Though this path formally achieves a higher order of accuracy, its practical utility is very limited because it unavoidably leads to expansion of the computational stencil within the *stiff* balance of (1.1) and (1.4), which is undesirable, especially in the horizontal direction. This is an attempt to increase accuracy of horizontal and vertical discretizations *independently.* Another obstacle with this approach is that high-order polynomial fits tend to oscillate in the vicinity of sharp changes of gradients of the interpolated field. This problem, as we will see in the next section, can be essentially solved by employing appropriate constraining techniques. Such non-oscillatory algorithms are possible only for the density field, since there is a natural limitation of vertical density gradient associated with neutral stratification: the interpolant is not allowed to have derivative opposite in sign to the elementary difference of nearest points[2]. In an attempt to do so for P, one needs to impose constraints on the second derivatives, which is more difficult to implement.

In the present study we chose an alternative path that leads to the possibility of canceling hydrostatic error using a two-point stencil in the horizontal direction.

Eqn. (2.5) is often viewed as a second-order discrete approximation to the hydrostatic equation. However, there are two ways to interpret gridded data: as a set of values of the function at *sampling* points (i.e., grid nodes); or as a set of averages of the function over grid boxes (i.e., control volumes). Within the second order of accuracy the two interpretations are undistinguishable, but not beyond the second order. The control-volume methods are most appropriate for the conservation laws, and they are commonly used in ocean models for discretization of advective terms in tracer and horizontal momentum equations. Therefore, we chose to interpret the discretized density

[2]For the sake of simplicity, here we temporarily neglect the distinction between *in situ* density and *potential* density. In the case of neutral stratification *in situ* density still increases with depth because of effects of compressibility. This will be reconsidered in Section 6.

should be also computed using quintic rule,

$$FC'_{i+\frac{1}{2},k+\frac{1}{2}} = \frac{1}{2}\Delta z_{i+\frac{1}{2},k+\frac{1}{2}}\Bigg[P_{i+1,k+\frac{1}{2}}+P_{i,k+\frac{1}{2}}+ \\ +\frac{1}{5}g\Delta z_{i+\frac{1}{2},k+\frac{1}{2}}\Bigg(\rho_{i+1,k+\frac{1}{2}}-\rho_{i,k+\frac{1}{2}}- \\ -z_{i+\frac{1}{2},k+\frac{1}{2}}\frac{d_{i+1,k+\frac{1}{2}}+d_{i,k+\frac{1}{2}}}{12}\Bigg)\Bigg], \tag{3.14}$$

as the alternative to the first two lines in (3.11).

Obviously, both (3.11) and (3.14) are derived under assumption that pressure, density and derivatives of density are related via hydrostatic balance, even thought the corresponding vertices do not belong to the same vertical column, like in the case of (3.6) and (3.7). Therefore, inclusion of the extra terms into (3.11) and (3.14) in comparison with Lin's trapezoidal integration rule would not reduce the error of approximation of FC', unless it is verified that the hydrostatic hypothesis holds, which may, or may not be the case, depending on dynamical situation.

To find how close it is to the hydrostatic balance, we compare two quantities,

$$\Delta P = P_{i,k+\frac{1}{2}} - P_{i+1,k+\frac{1}{2}} \tag{3.15}$$

and

$$\Delta m = \frac{1}{2}g\Delta z_{i+\frac{1}{2},k+\frac{1}{2}}\Big[\rho_{i,k+\frac{1}{2}} + \rho_{i+1,k+\frac{1}{2}} \\ -\frac{1}{6}\Delta z_{i+\frac{1}{2},k+\frac{1}{2}}\Big(d_{i+1,k+\frac{1}{2}} - d_{i,k+\frac{1}{2}}\Big)\Big], \tag{3.16}$$

which are the difference in pressure between the points $z_{i,k+\frac{1}{2}}$ and $z_{i+1,k+\frac{1}{2}}$ and cubic approximation to integral of density field, which is equivalent to the weight of water column of height $z_{i,k+\frac{1}{2}} - z_{i+1,k+\frac{1}{2}}$. In the case of hydrostatic balance these two should agree,

$$\Delta P \approx \Delta m\,. \tag{3.17}$$

Therefore we introduce a limiting function

$$f = \frac{2\Delta P\cdot\Delta m}{\Delta P^2+\Delta m^2} \quad \text{if} \quad \Delta P\cdot\Delta m > 0 \\ \text{and} \quad f=0 \quad \text{if otherwise,} \tag{3.18}$$

which is then used to modulate $\frac{1}{6}g\Delta z\Big(...\Big)$ and $\frac{1}{5}g\Delta z\Big(...\Big)$ terms in (3.11) and (3.14) respectively, so that the high-order correction terms are dropped once the two vertical columns are no longer in hydrostatic balance.

The choice of limiting function is, in principle, not unique. The above limiter can be rewritten as

$$f(\epsilon) = \frac{\epsilon+|\epsilon|}{1+\epsilon^2}\,, \tag{3.19}$$

where $\epsilon = \Delta m/\Delta P$, which is commonly known as van Leer limiter. It has the symmetry $f(1/\epsilon) = f(\epsilon)$, and the property that

$$\left.\frac{\partial f}{\partial \epsilon}\right|_{\epsilon=1} = 0\,, \tag{3.20}$$

which means that the modified (3.14) does not "give up" high-order correction terms, if violations of hydrostatic balance are relatively small.

The effect and necessity of such limiting will be fully investigated later in this study. At this moment we just emphasize that in the case of coarse resolution the actual order of accuracy drops down to that of Lin's algorithm, which is probably the best choice under such circumstances, because the mismatch in (3.17) is caused by either significant physical pressure gradient exceeding the hydrostatic pressure gradient error, or by spurious oscillations of high-order polynomial interpolants, which are therefore detected and prevented.

When stratification is not at rest, $PGF'_{i+\frac{1}{2},k}$ still approximates PGF with second-order accuracy. To verify it, we first note that

$$PGF_{i+\frac{1}{2},k} = -\frac{1}{2}\left(H_{i+1,k}+H_{i,k}\right)\Delta x \left.\frac{\partial P}{\partial x}\right|_{\substack{z=\text{const}\\ i+\frac{1}{2},k}}, \tag{3.21}$$

where $\frac{1}{2}\left(H_{i+1,k}+H_{i,k}\right)\Delta x$ is the volume of grid box around $u_{i+\frac{1}{2},k}$. Then we note that the remaining term in $PGF_{i+\frac{1}{2},k}$, missing in $PGF'_{i+\frac{1}{2},k}$, is

$$\frac{\Delta x}{12}\Big[\Big(z_{i+1,k+\frac{1}{2}}-z_{i,k+\frac{1}{2}}\Big)\Big(PX_{i+1,k+\frac{1}{2}}-PX_{i,k+\frac{1}{2}}\Big) - \\ -\Big(z_{i+1,k-\frac{1}{2}}-z_{i,k-\frac{1}{2}}\Big)\Big(PX_{i+1,k-\frac{1}{2}}-PX_{i,k-\frac{1}{2}}\Big)\Big] \\ \approx \frac{\Delta x^3\Delta z_{i+\frac{1}{2},k}}{12}\cdot\frac{\partial}{\partial z}\left[\left.\frac{\partial z}{\partial x}\right|_{s=\text{const}}\cdot\left.\frac{\partial PX}{\partial x}\right|_{s=\text{const}}\right], \tag{3.22}$$

where $\Delta z_{i+\frac{1}{2},k} = \frac{1}{2}\left(H_{i+1,k}+H_{i,k}\right)$ and

$$PX \equiv \left.\frac{\partial P}{\partial x}\right|_{z=\text{const}}$$

from (3.21) is

$$PX_{i+\frac{1}{2},k} = \frac{-PGF_{i+\frac{1}{2},k}}{\Delta z_{i+\frac{1}{2},k}\Delta x}\,. \tag{3.23}$$

Since (3.22) divided by $\Delta z_{i+\frac{1}{2},k}\Delta x$ is the error term in computing $PX_{i+\frac{1}{2},k}$, we see that

$$PX \ll \Delta x^2\frac{r}{12}\cdot\frac{\partial}{\partial z}\left[\left.\frac{\partial z}{\partial x}\right|_{s=\text{const}}\cdot\left.\frac{\partial PX}{\partial x}\right|_{s=\text{const}}\right] \tag{3.24}$$

tonicity, minimal quadratic variance of the field and its derivatives, etc. It is often the case when some of these properties cannot be satisfied simultaneously (e.g., attempt to maintain continuity of derivatives causes spurious oscillations of the interpolant; while enforcement of monotonicity destroys smoothness and/or continuity), therefore we advocate the development of adaptive techniques based on hierarchy of principles in such a way one may override the other in the case of conflict. This leads to multistage methods where the order polynomial interpolant increases gradually in such a way that the lower order method provides both initial estimate of interfacial values and the criterion of smoothenss, which locally restricts the higher order method to avoid undesirable oscillations.

In this study we presume that density is a physically continuous field, so we made no effort to obtain shock-capturing capability for our methods (which in principle can be done). Neither we focus our attention on accurate treatment of extrema, since in a hydrostatic ocean model density is expected to be positively stratified, and any violation of this is considered as transient. We design our methods to be accurate on spatially nonuniform vertical grids, because the use of such grids is physically motivated in ocean modeling and is part of everyday practice.

4.2. Basic Parabolic Spline

Consistently with the finite volume approach we interpret the set of values $\{\overline{\rho}_k \,|\, k=1,\dots N\}$ as a set of grid-box-averaged values of the density field. Furthermore, we assume parabolic distributions of density within each grid box,

$$\rho(z') = \rho_{k+\frac{1}{2}}\left(\frac{1}{2}+\frac{z'}{H_k}\right)+\rho_{k-\frac{1}{2}}\left(\frac{1}{2}-\frac{z'}{H_k}\right) \\ +6\left(\frac{\rho_{k+\frac{1}{2}}+\rho_{k-\frac{1}{2}}}{2}-\overline{\rho}_k\right)\left(\frac{z'^2}{H_k^2}-\frac{1}{4}\right) . \tag{4.2}$$

where z' is a local vertical coordinate, $-H_k/2 \le z' \le +H_k/2$, defined separately within each grid box H_k, $k=1,\dots N$; and $\rho_{k\pm\frac{1}{2}}$ are the interfacial values which are yet to be determined. Obviously from (4.2),

$$\rho(\pm H_k/2) = \rho_{k\pm\frac{1}{2}} , \tag{4.3}$$

and one can immediately verify that

$$\frac{1}{H_k}\int_{-H_k/2}^{+H_k/2}\rho(z')\,dz' \equiv \overline{\rho}_k , \tag{4.4}$$

Eq. (4.2) already guarantees that the reconstructed density profile (which consists of parabolic segments within each grid box) is continuous, since all $\rho_{k\pm\frac{1}{2}}$, $k=1,\dots N-1$are "shared" by the adjacent grid boxes H_k and H_{k+1}. Furthermore, $\rho_{k\pm\frac{1}{2}}$ will be chosen from the condition of continuity of the first derivative across the grid box interfaces.

Differentiation of (4.2) with respect to z' results in

$$d(z') \equiv \frac{\partial\rho}{\partial z}(z') = \frac{\rho_{k+\frac{1}{2}}-\rho_{k-\frac{1}{2}}}{H_k} + \\ +12\left(\frac{\rho_{k+\frac{1}{2}}+\rho_{k-\frac{1}{2}}}{2}-\overline{\rho}_k\right)\frac{z'}{H_k^2} , \tag{4.5}$$

which has the following values at the upper and lower facets of the grid box H_k,

$$d\Big(+\frac{H_k}{2}\Big) = +\frac{4\rho_{k+\frac{1}{2}}+2\rho_{k-\frac{1}{2}}-6\overline{\rho}_k}{H_k} \tag{4.6}$$

$$d\Big(-\frac{H_k}{2}\Big) = -\frac{2\rho_{k+\frac{1}{2}}+4\rho_{k-\frac{1}{2}}-6\overline{\rho}_k}{H_k} . \tag{4.7}$$

Continuity of the first derivative across the grid box interfaces $k+\frac{1}{2}$ requires that,

$$\frac{4\rho_{k+\frac{1}{2}}+2\rho_{k-\frac{1}{2}}-6\overline{\rho}_k}{H_k} = -\frac{2\rho_{k+\frac{3}{2}}+4\rho_{k+\frac{1}{2}}-6\overline{\rho}_{k+1}}{H_{k+1}} , \tag{4.8}$$

which leads to the following tri-diagonal system of equations for the interfacial values $\overline{\rho}_{k+\frac{1}{2}}$, $k=1,\dots,N-1$:

$$H_{k+1}\rho_{k-\frac{1}{2}} + 2\big(H_{k+1}+H_k\big)\rho_{k+\frac{1}{2}} + H_k\rho_{k+\frac{3}{2}} \\ = 3\big(H_{k+1}\overline{\rho}_k + H_k\overline{\rho}_{k+1}\big) . \tag{4.9}$$

Eqs. (4.9) requires two boundary conditions at $k=1$ and $k=N$. These boundary conditions may be either physically motivated (e.g., a Neumann condition, which stems from no-flux condition), or, if formulation of physical boundary condition is impossible, an appropriate extrapolation rule may be employed (this is equivalent to local reduction of the order of accuracy in the vicinity of the boundary). Plausible choices are the following:

Dirichlet:

$$\rho_{\frac{1}{2}} \ , \ \ \rho_{N+\frac{1}{2}} \quad \text{are prescribed} . \tag{4.10}$$

Neumann, [which are derived from Eqs. (4.6)–(4.7) by setting l.h.s. to zero (or a prescribed value)]:

$$\rho_{\frac{1}{2}} + \frac{1}{2}\rho_{\frac{3}{2}} = \frac{3}{2}\overline{\rho}_1 , \qquad \rho_{N+\frac{1}{2}} + \frac{1}{2}\rho_{N-\frac{1}{2}} = \frac{3}{2}\overline{\rho}_N . \tag{4.11}$$

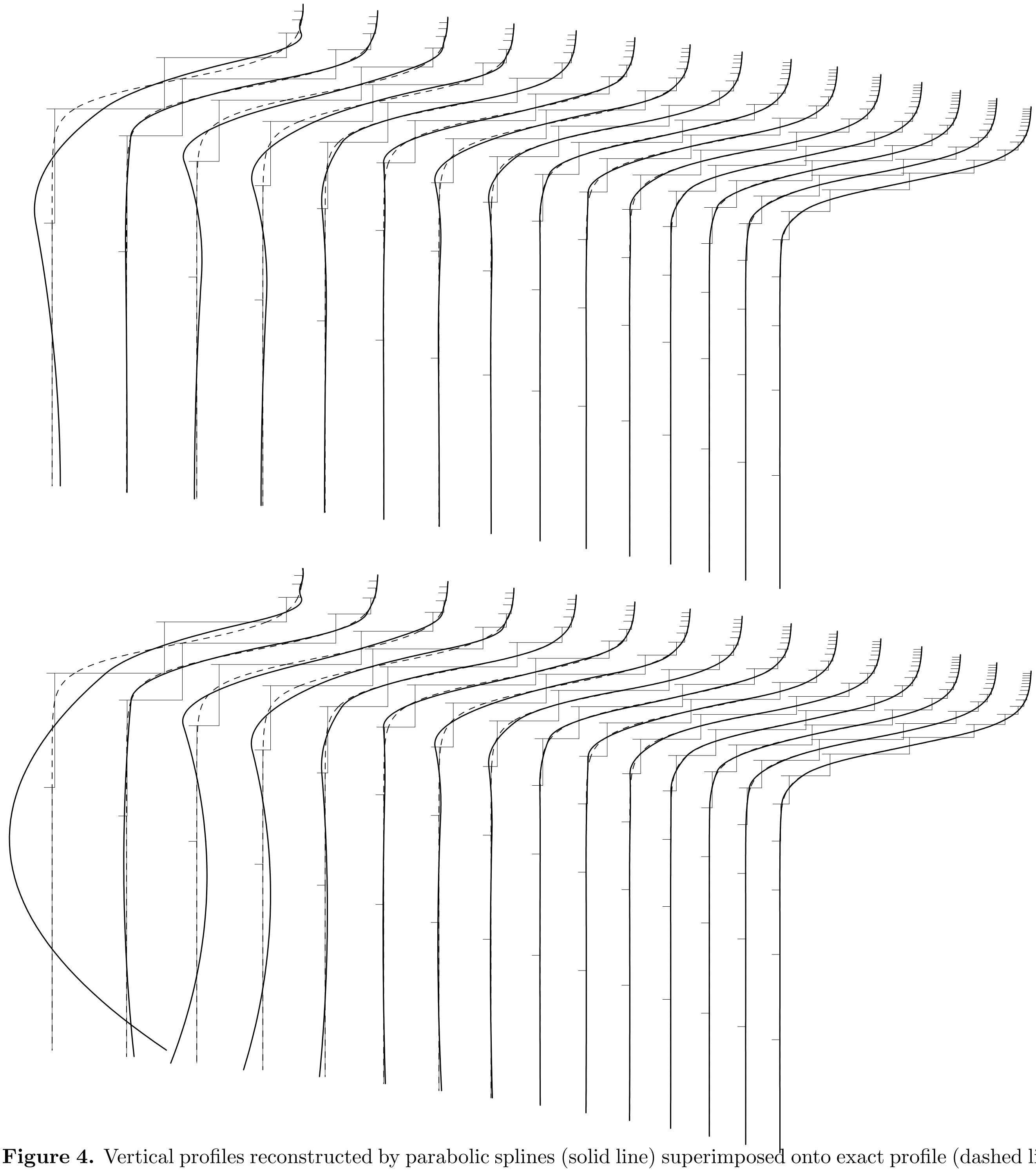

Figure 4. Vertical profiles reconstructed by parabolic splines (solid line) superimposed onto exact profile (dashed line). The fifteen curves on each panel from left to right correspond to vertical resolutions of $N = 7, \dots 21$ where N is the number of grid boxes of a nonuniform grid. The grid box interfaces are shown by horizontal tick marks, while vertical straight line in each box corresponds to the box-averaged values. **Upper panel** — Neumann boundary conditions at top and bottom; **Lower panel** — Same as above, but quadratic extrapolation rule is used instead. To avoid graphical interference between the curves, we have inverted density (so the field shown here is actually $-\rho$, or "buoyancy"). For the same reason the profiles are shifted downward when going from left to right.

Similarly, for the third derivative we find

$$\left.\frac{\partial^3\rho}{\partial z'^3}\right|_{z'=+H_k/2} = \frac{24}{H_k^3}\left[-8\rho_{k+\frac{1}{2}} - 7\rho_{k-\frac{1}{2}} + 15\overline{\rho}_k + \right. \tag{4.29}$$

$$\left. + H_k\left(\frac{3}{2}d_{k+\frac{1}{2}} - d_{k-\frac{1}{2}}\right)\right]$$

$$\left.\frac{\partial^3\rho}{\partial z'^3}\right|_{z'=-H_k/2} = \frac{24}{H_k^3}\left[7\rho_{k+\frac{1}{2}} + 8\rho_{k-\frac{1}{2}} - 15\overline{\rho}_k - \right. \tag{4.30}$$

$$\left. - H_k\left(d_{k+\frac{1}{2}} - \frac{3}{2}d_{k-\frac{1}{2}}\right)\right]$$

which leads to the matching condition,

$$7\frac{\rho_{k-\frac{1}{2}}}{H_k^3} + 8\left(\frac{1}{H_{k+1}^3} + \frac{1}{H_k^3}\right)\rho_{k+\frac{1}{2}} + 7\frac{\rho_{k+\frac{3}{2}}}{H_{k+1}^3} +$$

$$+\frac{d_{k-\frac{1}{2}}}{H_k^2} + \frac{3}{2}\left(\frac{1}{H_{k+1}^2} - \frac{1}{H_k^2}\right)d_{k+\frac{1}{2}} - \frac{d_{k+\frac{3}{2}}}{H_{k+1}^2} = \tag{4.31}$$

$$= 15\left(\frac{\overline{\rho}_{k+1}}{H_{k+1}^3} + \frac{\overline{\rho}_k}{H_k^3}\right),$$

Since (4.28)–(4.31) exist only for $k = 1, ..., N-1$, two side boundary conditions are required for $\rho_{\frac{1}{2}}$, $d_{\frac{1}{2}}$ and $\rho_{N+\frac{1}{2}}$, $d_{N+\frac{1}{2}}$. Similarly to parabolic spline reconstruction, these boundary conditions may be provided by the physics, or they may be just extrapolation rules. Eqs. (4.28)–(4.31) along with the two pairs of boundary conditions require a block tri-diagonal solver in each vertical column.

Although descriptions of such solvers are available in the literature, cf. Chu & Fan, 1998, we discuss it here for the following reasons: First, one needs to assess its computational cost and provisional storage requirements in order to construct an efficient algorithm, which is competitive with the alternatives from the practical point view. Specifically, we advocate a specialized algorithm which computes associated matrices of coefficients "on fly" during the block-gaussian elimination procedure, rather than building an interface to a standard algorithm, which is then used as a "black box". Second, later in this study we will introduce a nonlinear weighting procedure to control oscillations of the resultant quartic spline, which becomes an inseparable part of the solver.

We note that the system of (4.28)–(4.31) may be rewritten in matrix form as

$$\mathbf{A}_k \cdot \mathbf{r}_{k-\frac{1}{2}} + \mathbf{B}_{k+\frac{1}{2}} \cdot \mathbf{r}_{k+\frac{1}{2}} + \mathbf{A}'_{k+1} \cdot \mathbf{r}_{k+\frac{3}{2}} = \mathbf{d}_{k+\frac{1}{2}}\,, \tag{4.32}$$

where $\mathbf{A}$, $\mathbf{A}'$ and $\mathbf{B}$ are 2×2 matrices,

$$\mathbf{A}_k \equiv \begin{pmatrix} (a_{11})_k & (a_{12})_k \\ (a_{21})_k & (a_{22})_k \end{pmatrix} = \begin{pmatrix} -\frac{2}{5H_k^2} & -\frac{1}{20H_k} \\ \frac{7}{15H_k^3} & \frac{1}{15H_k^2} \end{pmatrix} \tag{4.33}$$

$$\mathbf{A}'_{k+1} = \begin{pmatrix} -(a_{11})_{k+1} & (a_{12})_{k+1} \\ (a_{21})_{k+1} & -(a_{22})_{k+1} \end{pmatrix} \tag{4.34}$$

$$\mathbf{B}_{k+\frac{1}{2}} = \begin{pmatrix} (b_{11})_{k+\frac{1}{2}} & (b_{12})_{k+\frac{1}{2}} \\ (b_{21})_{k+\frac{1}{2}} & (b_{22})_{k+\frac{1}{2}} \end{pmatrix} = \tag{4.35}$$

$$= \begin{pmatrix} \frac{3}{2}\left[(a_{11})_k - (a_{11})_{k+1}\right] & -3\left[(a_{12})_k + (a_{12})_{k+1}\right] \\ \frac{8}{7}\left[(a_{21})_k + (a_{21})_{k+1}\right] & -\frac{3}{2}\left[(a_{22})_k - (a_{22})_{k+1}\right] \end{pmatrix},$$

$\mathbf{r}$ in unknown 2-vector,

$$\mathbf{r}_{k+\frac{1}{2}} \equiv \begin{pmatrix} (r_1)_{k+\frac{1}{2}} \\ (r_2)_{k+\frac{1}{2}} \end{pmatrix} = \begin{pmatrix} \rho_{k+\frac{1}{2}} \\ d_{k+\frac{1}{2}} \end{pmatrix} \tag{4.36}$$

and $\mathbf{d}$ is known 2-vector of r.h.s.,

$$\mathbf{d}_{k+\frac{1}{2}} \equiv \begin{pmatrix} (d_1)_{k+\frac{1}{2}} \\ (d_2)_{k+\frac{1}{2}} \end{pmatrix} = \begin{pmatrix} \frac{\overline{\rho}_{k+1}}{H_{k+1}^2} - \frac{\overline{\rho}_k}{H_k^2} \\ \frac{\overline{\rho}_{k+1}}{H_{k+1}^3} + \frac{\overline{\rho}_k}{H_k^3} \end{pmatrix}. \tag{4.37}$$

Suppose the lower boundary condition for (4.32) exists in the form,

$$\mathbf{r}_{\frac{1}{2}} + \mathbf{C}_{\frac{1}{2}} \cdot \mathbf{r}_{\frac{3}{2}} = \mathbf{d}^*_{\frac{1}{2}}\,, \tag{4.38}$$

where $\mathbf{C}_{\frac{1}{2}}$ is a known 2×2 matrix, $\mathbf{d}^*_{\frac{1}{2}}$ is known 2-vector, $\mathbf{r}_{\frac{1}{2}}$ and $\mathbf{r}_{\frac{3}{2}}$ are unknown vectors (the possible settings of $\mathbf{C}_{\frac{1}{2}}$ and $\mathbf{d}^*_{\frac{1}{2}}$ in (4.38) will be discussed below). This equation serves as a starting point for the block tri-diagonal gaussian elimination procedure. It can be viewed as the $k = 1$ equation among the partially solved (4.32),

$$\mathbf{r}_{k-\frac{1}{2}} + \mathbf{C}_{k-\frac{1}{2}} \cdot \mathbf{r}_{k+\frac{1}{2}} = \mathbf{d}^*_{k-\frac{1}{2}}\,, \tag{4.39}$$

where $k = 1, \ldots N$. Starting from $k = 2$ and all the way to $k = N-1$, coefficient matrices $\mathbf{C}_{k+\frac{1}{2}}$ and $\mathbf{d}^*_{k+\frac{1}{2}}$ are obtained from $\mathbf{C}_{k-\frac{1}{2}}$ and $\mathbf{d}^*_{k-\frac{1}{2}}$ as follows.

Multiplying (4.39) by $\mathbf{A}_k$ from the left and subtracting it from (4.32), one can eliminate $\mathbf{r}_{k-\frac{1}{2}}$,

$$\left(\mathbf{B}_{k+\frac{1}{2}} - \mathbf{A}_k \cdot \mathbf{C}_{k-\frac{1}{2}}\right) \cdot \mathbf{r}_{k+\frac{1}{2}} + \mathbf{A}'_{k+1} \cdot \mathbf{r}_{k+\frac{3}{2}} = \tag{4.40}$$

$$= \mathbf{d}_{k+\frac{1}{2}} - \mathbf{A}_k \cdot \mathbf{d}^*_{k-\frac{1}{2}}\,.$$

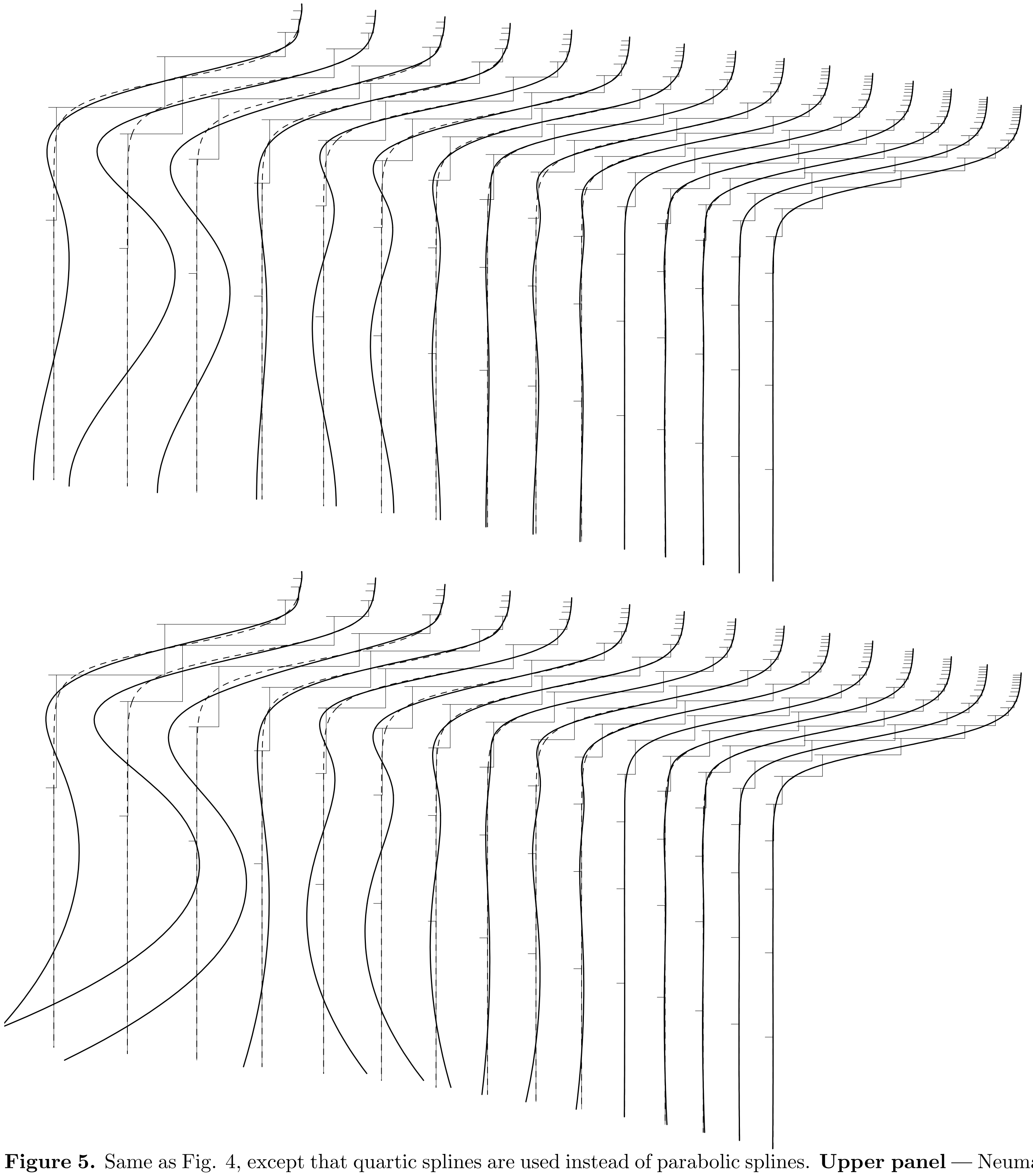

Figure 5. Same as Fig. 4, except that quartic splines are used instead of parabolic splines. **Upper panel** — Neumann B.C.; **Lower panel** — quadratic truncation rule.

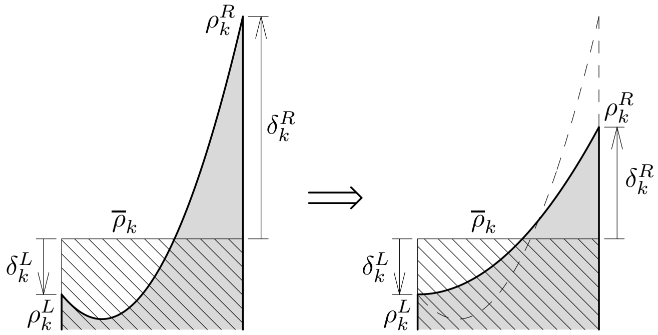

Figure 6. PPM monotonicity constraint. Shaded area under parabola (which is equal to the area of rectangle covered by diagonal lines) is conserved after the larger in absolute value of δ_k^R or δ_k^L is restricted to be no more than twice the smaller one (in this example it is δ_k^R which is restricted).

$$+6\left(\frac{\rho_k^R+\rho_k^L}{2}-\overline{\rho}_k\right)\left(\frac{z'^2}{H_k^2}-\frac{1}{4}\right) .$$

where ρ_k^R and ρ_k^L are the upper and lower limits of the distribution inside grid box H_k (which are analogous to $a_{R,j}$ and $a_{L,j}$ in Colella & Woodward, 1984).

By its construction, PPM does not guarantee continuity of the first derivative across the grid box interface. If none of the conditions in reset-restrict conditions in (4.58) holds, it is obvious that $\rho_k^L = \rho_{k-\frac{1}{2}}$ and $\rho_k^R = \rho_{k+\frac{1}{2}}$, so that the resultant interpolant is continuous. However, after (4.58), it is no longer guaranteed, since it becomes possible that $\rho_k^R \neq \rho_{k+1}^L$. It is guaranteed, however, that either

$$\overline{\rho}_k \le \rho_k^R \le \rho_{k+1}^L \le \overline{\rho}_{k+1} \, , \qquad (4.60)$$

or

$$\overline{\rho}_k \ge \rho_k^R \ge \rho_{k+1}^L \ge \overline{\rho}_{k+1} \, , \qquad (4.61)$$

and therefore the reconstructed profile is monotonic even in the presense of discontinuity.

It is instructive to see the effect of all steps of PPM. First, we turn off all constraining algorithms, see Fig. 7. In comparison to the profiles obtained by parabolic splines, local polynomial fit shows slower convergence, despite the same order of accuracy in the sense of a Taylor series analysis. A comparison with Fig. 4 shows that the profiles in the right half of the top panel in Fig. 7 still exhibit the wrong sign of curvature within the grid boxes, as well as a significant jump in the first derivative, while the spline profiles are smooth and are much closer to the ideal curve with similar resolution. Slope limiting (Fig. 7) lower panel, eliminates most of the oscillations, while the internal monotonicity constraint (4.58) removes the remaining oscillations at the expense of continuity of the profile, Fig. 8.

It is generally recognized that PPM has tendency to underestimate the slope and curvature within the grid box in the event when limiting has effect. This results in discontinuity of the reconstructed profile often in the cases when the discontinuity is not associated with any physical discontinuity (such as a shock) and, in principle, the profile can be reconstructed are a set of continuously matched monotonic parabolic segments. To address the issue, various enhancement algorithms to PPM were devised. This procedure is often known as steepening. A simple (though not the most efficient) enhancement algorithm of this kind consists of setting

$$\rho_{k+\frac{1}{2}} = \frac{\rho_k^R+\rho_{k+1}^L}{2} \qquad k=2,\ldots,N-1 \, , \qquad (4.62)$$

and then repeating operations (4.62)—(4.58) iteratively. This procedure results in reduction of the discontinuities, while maintaining strict monotonicity of the profile. The convergence is relatively fast and only few steps are required. This procedure "patches up" the gaps, making the profile close to the ideal line, especially for coarse resolution, Fig. 8, lower panel.

Since PPM slope-limiting procedure produces reasonably accurate interfacial values (Fig. 7, lower panel) another potentially attractive possibility is to compute interfacial derivatives from the same *limited* polynomial interpolants and the approximate density distribution inside grid boxes by quartic (rather than parabolic) polynomials. This leads to a pseudo-spline algorithm, where value and first derivative are continuous across grid-box interfaces.

The quartic polynomial fit for the indefinite integral of density $\rho(z)$ (cf. Colella & Woodward, 1984) may be obtained via *reconciliation* of lower order interpolants,

$$\begin{aligned}\mathcal{Q}(z'') = \mathcal{P}_k(z'')\frac{H_{k+1}+H_{k+2}-z''}{H_{k-1}+H_k+H_{k+1}+H_{k+2}} \qquad (4.63)\\ +\mathcal{P}_{k+1}(z'')\frac{z''+H_k+H_{k-1}}{H_{k-1}+H_k+H_{k+1}+H_{k+2}}\end{aligned}$$

where $\mathcal{P}_k(z'')$ and $\mathcal{P}_{k+1}(z'')$ are cubic polynomial inter-

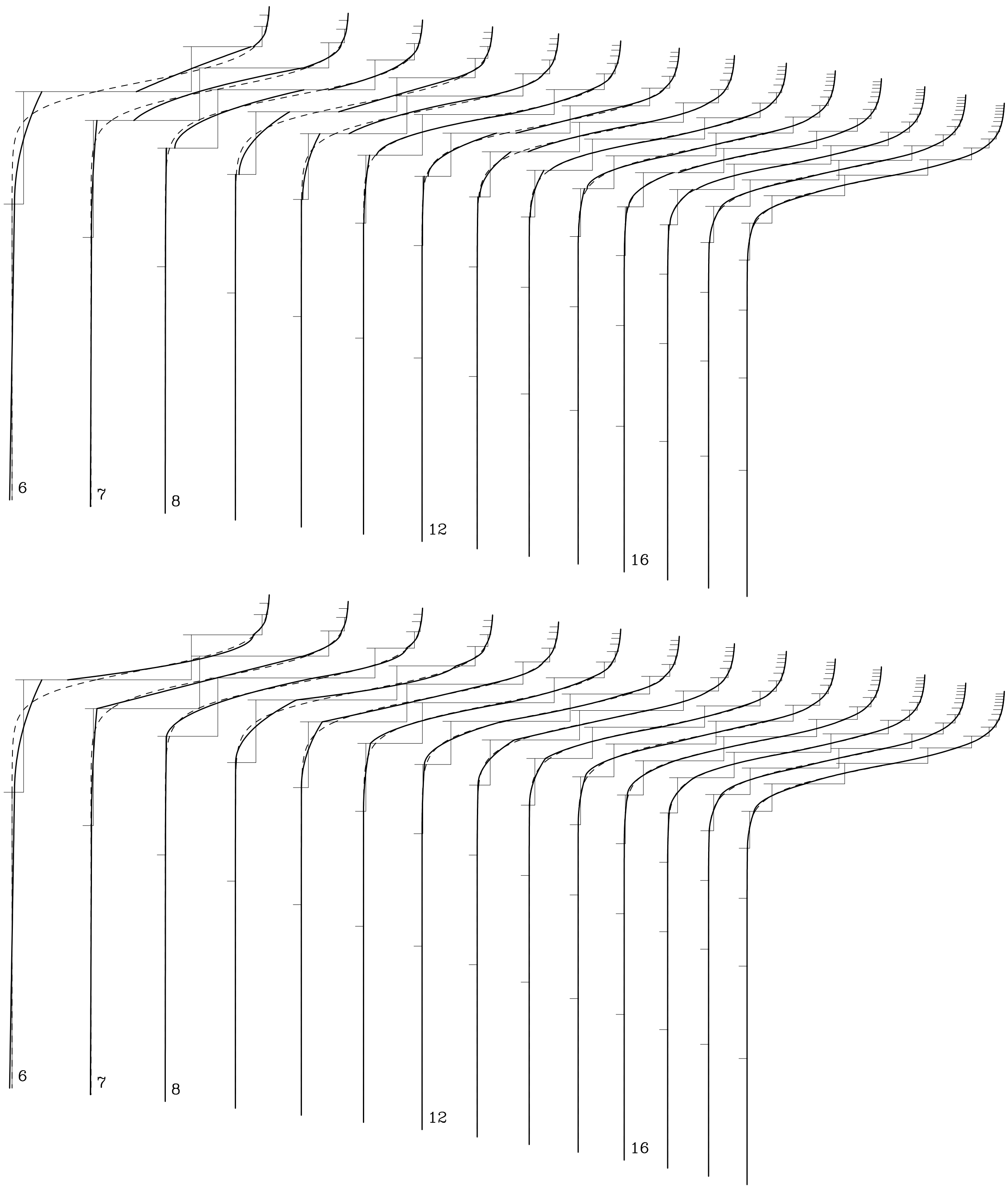

Figure 8. Same as Fig. 7, except that **Upper panel** — both monotonicity constraints [Eqs. (1.8) and (1.10) in Colella & Woodward (1984)] are now applied; **Lower panel** — iteratively enhanced PPM profiles.

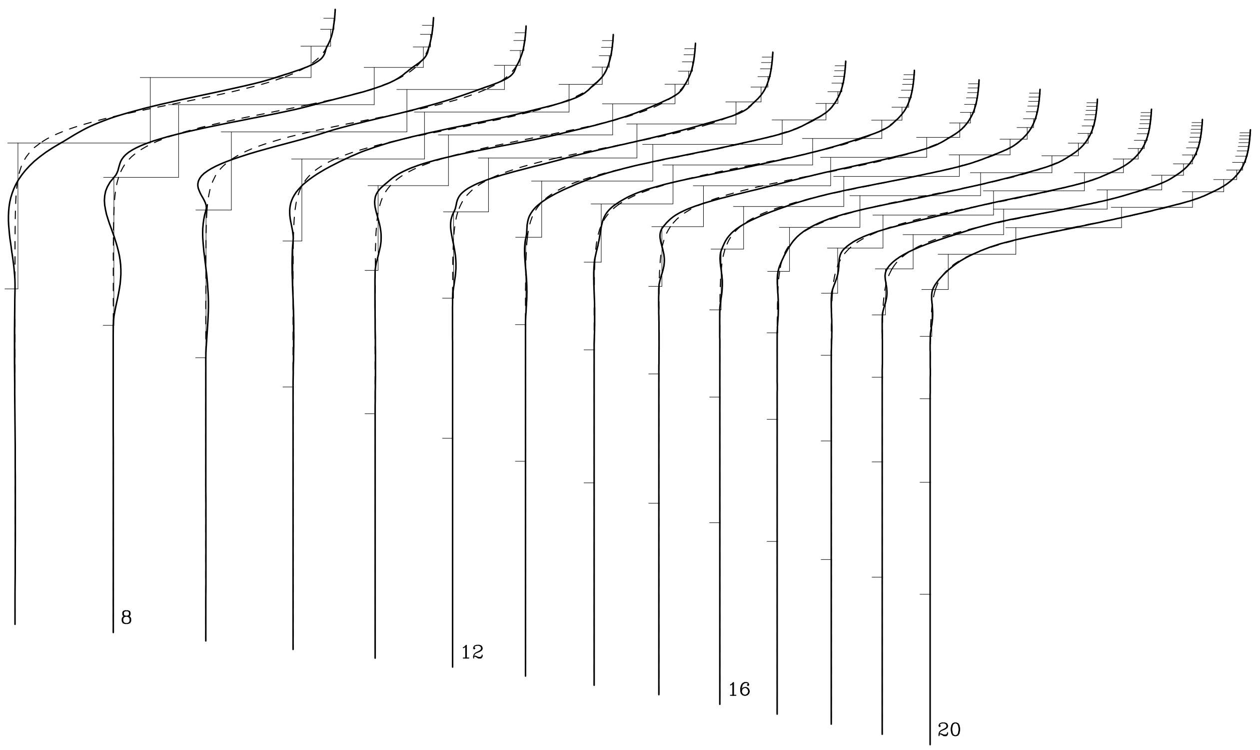

Figure 9. Vertical profiles reconstructed by Limited Quartic Pseudo-spline. Despite the fact that it guarantees that all interfacial values fall within the bounds set by adjacent grid box values and all interfacial derivatives have correct sign, oscillations of the interplant are present at coarse resolution.

therefore as long as $d^{(0)}_{k+\frac{1}{2}}$ and $d^{(0)}_{k-\frac{1}{2}}$ are of the same sign, it is already guaranteed that δ^R_k and δ^L_k also have the same sign. Consequently to enforce (4.71) is sufficient to restrict

$$\left|\delta^R_k\right| \le (H_k + H_{k+1}) \left|d^{(0)}_{k+\frac{1}{2}}\right| \qquad\qquad (4.73)$$
$$\left|\delta^L_k\right| \le (H_{k-1} + H_k) \left|d^{(0)}_{k-\frac{1}{2}}\right| ,$$

which, after substitution of expressions for $\delta^{L,R}_k$ becomes

$$H_k \left|d^{(0)}_{k+\frac{1}{2}}\right| \le (H_{k-1} + 2H_k + H_{k+1}) \left|d^{(0)}_{k-\frac{1}{2}}\right| \qquad\qquad (4.74)$$
$$H_k \left|d^{(0)}_{k-\frac{1}{2}}\right| \le (H_{k-1} + 2H_k + H_{k+1}) \left|d^{(0)}_{k+\frac{1}{2}}\right| .$$

(Recall that in the case of uniform grid this is equivalent to the constraint that successive differences should not differ by more than 4 times, cf. Eq. (1.8) from Colella & Woodward, 1984.) The limited version of (4.68)–(4.69) is therefore formulated as the following algorithm,

$$\delta^{R\prime}_k = \text{minmod}\left(H_k d^{(0)}_{k+\frac{1}{2}} \, , \Delta_4 d^{(0)}_{k-\frac{1}{2}}\right) \qquad\qquad (4.75)$$
$$\delta^{L\prime}_k = \text{minmod}\left(H_k d^{(0)}_{k-\frac{1}{2}} \, , \Delta_4 d^{(0)}_{k+\frac{1}{2}}\right)$$

where

$$\Delta_4 = H_{k-1} + 2H_k + H_{k+1} \qquad\qquad (4.76)$$

and minmod is a function of two or more arguments, which is equal the argument smallest by absolute value, if all arguments have the same sign; or equal to zero, some of its arguments have different sign. The interfacial deviations become

$$\delta^R_k = \delta^{R\prime}_k - H_{k-1}\gamma'_k \qquad\qquad (4.77)$$
$$\delta^L_k = \delta^{L\prime}_k + H_{k+1}\gamma'_k$$

where

$$\gamma'_k = \frac{\delta^{R\prime}_k - \delta^{L\prime}_k}{H_{k-1} + H_k + H_{k+1}} .$$

To prove that if $d^{(0)}_{k+\frac{1}{2}}$ and $d^{(0)}_{k-\frac{1}{2}}$ satisfy (4.74), then the resultant parabolic segment is monotone inside grid box H_k, it is sufficient to verify that

$$\frac{1}{2} \le \left|\frac{\delta^R_k}{\delta^L_k}\right| = \left| f\left(\frac{d^{(0)}_{k+\frac{1}{2}}}{d^{(0)}_{k-\frac{1}{2}}}\right)\right| \le 2 \qquad\qquad (4.78)$$

where, cf. (4.72),

$$f(x) = \frac{(H_{k-1} + H_k)\, x + H_{k+1}}{H_{k-1}x + H_k + H_{k+1}} . \qquad\qquad (4.79)$$

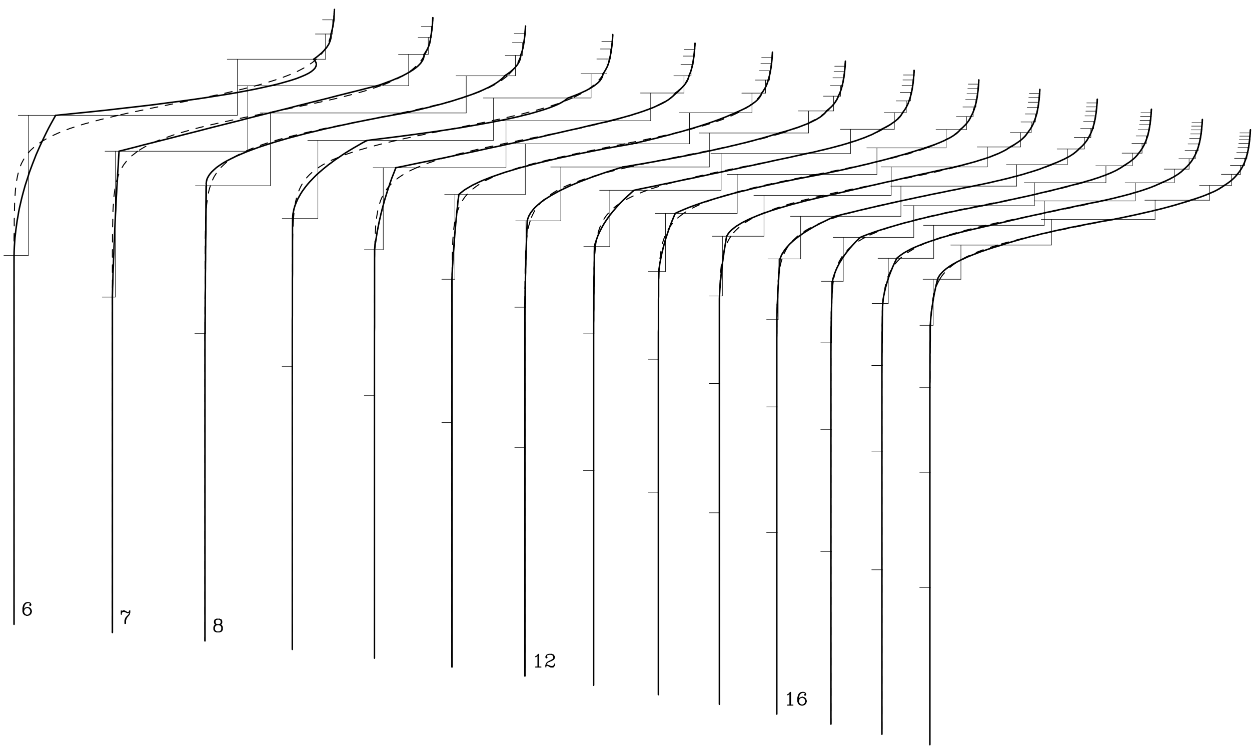

Figure 10. Profiles based on interfacial values obtained by Weighted ENO and assuming parabolic distributions within each grid box

.

self-similar grid stretching,

$$\frac{H_{k+1} + H_{k+2}}{H_{k-1} + H_k} \approx \left(\frac{H_{k+1}}{H_k}\right)^2 \tag{4.86}$$

(which is always the case if grid is generated by a sufficiently smooth mapping function) results in asymptotic accuracy similar to that of (4.65), which is higher that rate of any of the candidate interpolants. Choice of infinitely large n means accepting the value from the smoothest interpolant (all other candidate values are discarded), as it done in the original (non-weighred) ENO technique. This yields non-oscillatory behavior at coarse resolution, but also no gain in asymptotic convergence rate relatively to the order of accuracy of candidate stencil in the case of smooth field. Typically n is chosen from a compromise between desired asymptotic order of accuracy and robustness at coarse resolution [8].

[8]Strictly speaking the technique described here differs from the original (W)ENO by the fact slope limiting already involved in computation that the candidate interfacial values in (4.75)–(4.77). This limiting guarantees that both candidate values fall within the bounds set by the adjacent grid-box values, and because of convexity of (4.84), so does $\rho_{k+\frac{1}{2}}$. It also affects computation of weights, since variation of the parabolic segment within its grid box may be restricted. Classical bottom-up WENO schemes do not use such limiting, relying exclussively on measure of smoothness computed directly from the grid-box values.

Profiles produced by this algorithm with $n = 2$ are shown on Fig. 10 . The results are very similar to that of iterated PPM, see Fig. 8 , lower panel, but it is achieved only at a fraction of computational cost.

4.6. Parabolic Slope Reconciliation

Thus far it has been shown that in comparison with local polynomial fit, parabolic spline produces more accurate profiles in cases of moderate resolution. At the same time spline profiles exhibit oscillations if the resolution is too coarse, and there, unlike for the local methods, is no obvious way to control the oscillations. In this part we introduce a method which behaves almost like a spline for smooth profiles, and it also has the capability to prevent oscillations.

Alternatively to the tri-diagonal systems in Secs. 4.2 , a parabolic spline profile may be obtained by an iterative procedure. Suppose for a given set of $\{\overline{\rho}_k \,|\, k = 1, \dots, N\}$ there is exist a set of interfacial values $\left\{\rho_{k+\frac{1}{2}} \,|\, k = 0, \dots, N\right\}$. Then assuming that inside each grid box density distribution is approximated by a parabolic segment (4.2), one can find the mismatch of the left and right limits of the

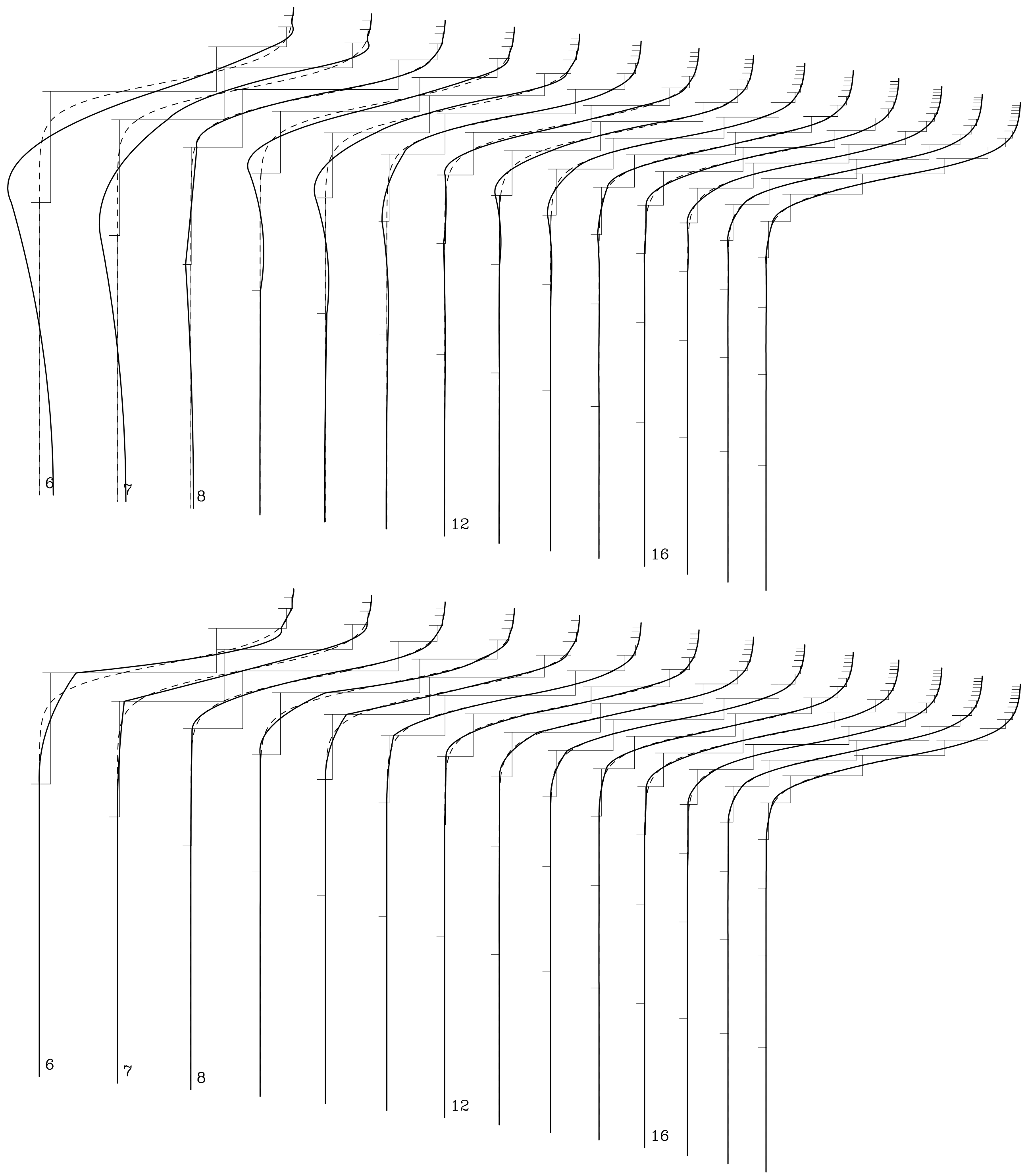

Figure 11. Vertical profiles reconstructed by Parabolic Slope Reconciliation: **Upper panel** — using two reconciliation steps and without any monotonicity constraints; **Lower panel** — same as above, but parabolic (like in PPM) limiters inside each grid box with subsequent reconciliation of interfacial values using weighting inversely proportional to internal quadratic variation. Note that continuity of the first derivative is not always guaranteed.

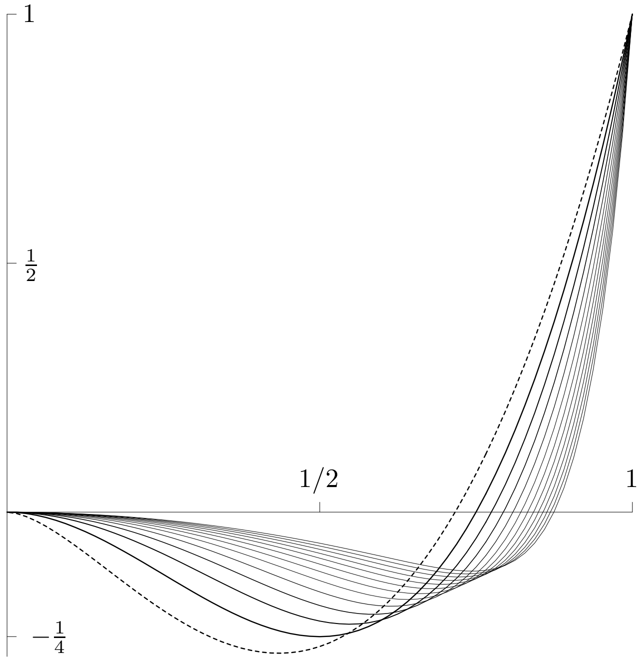

Figure 13. A family of replacement functions $\Phi_\beta(\xi)$ for $\beta = 0$ (thick dashed line) and $\beta = 1, 2, \ldots 12$ solid lines.

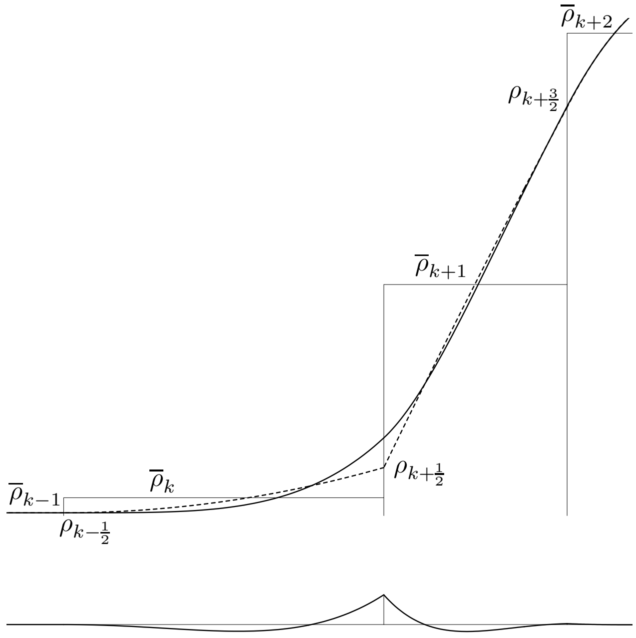

Figure 14. Dashed lines show original parabolic segments obtained by Weighted ENO. In this situation the discontinuity of the first derivative at the interface $k+\frac{1}{2}$ cannot be removed by modifying coefficients of the parabolic fits. Solid line – profile reconciled using power law. Note that in each grid box areas below solid and dashed lines are equal to each other. Shown on the bottom is the difference between solid and dashed profile.

so that there is no discontinuity in value at the interface $k+\frac{1}{2}$, and the side limit of the first derivative at $k+\frac{1}{2}$ is incremented by

$$-\frac{A(\beta+5)}{H_{k+1}}\,. \tag{4.107}$$

If amplitude of correction A and power β are chosen to satisfy

$$d^L_{k+1} - d^R_k = A(\beta+5)\left(\frac{1}{H_k} + \frac{1}{H_{k+1}}\right) \tag{4.108}$$

then the increments (4.105)–(4.107) cancel out the discontinuity of the first derivatives of parabolic distributions across the interface $k+\frac{1}{2}$, yielding the reconciled interfacial derivative,

$$d_{k+\frac{1}{2}} = \frac{H_k d^R_k + H_{k+1} d^L_{k+1}}{H_k + H_{k+1}}\,. \tag{4.109}$$

(In the derivation of (4.109) we have assumed that β is the same in both adjacent grid boxes.)

Because changing $\rho_{k+\frac{1}{2}}$ causes increase of variation in one of the adjacent grid boxes, H_k or H_{k+1}, in order to ensure monotonicity in *that* grid box we require that

$$\frac{1}{\beta}\,|A| \le \left|\overline{\rho}_k - \rho_{k-\frac{1}{2}}\right| \tag{4.110}$$

$$\left|d_{k+\frac{1}{2}}\right| \le 56\cdot\left|\frac{\overline{\rho}_k - \rho_{k-\frac{1}{2}}}{H_k}\right| \tag{4.111}$$

$$\frac{A(\beta+5)}{H_k} = d_{k+\frac{1}{2}} - d^R_k \tag{4.112}$$

if $\left(d^L_{k+1} - d^R_k\right)\left(\overline{\rho}_{k+1} - \overline{\rho}_k\right) > 0$, and

$$\frac{1}{\beta}\,|A| \le \left|\rho_{k+\frac{3}{2}} - \overline{\rho}_{k+1}\right| \tag{4.113}$$

$$\left|d_{k+\frac{1}{2}}\right| \le 56\cdot\left|\frac{\rho_{k+\frac{3}{2}} - \overline{\rho}_{k+1}}{H_{k+1}}\right| \tag{4.114}$$

$$\frac{A(\beta+5)}{H_{k+1}} = d^L_{k+1} - d_{k+\frac{1}{2}} \tag{4.115}$$

if otherwise.

The necessity of (4.111)—(4.114) will be explained later. Because in these unequalities all quantities except $d_{k+\frac{1}{2}}$ are assumed to be known, the only way satisfy one of them is to adjust $d_{k+\frac{1}{2}}$ by reducing it in its magnitude from the original value set by (4.109). In the case when $d_{k+\frac{1}{2}}$ retains its original value after the restriction, one

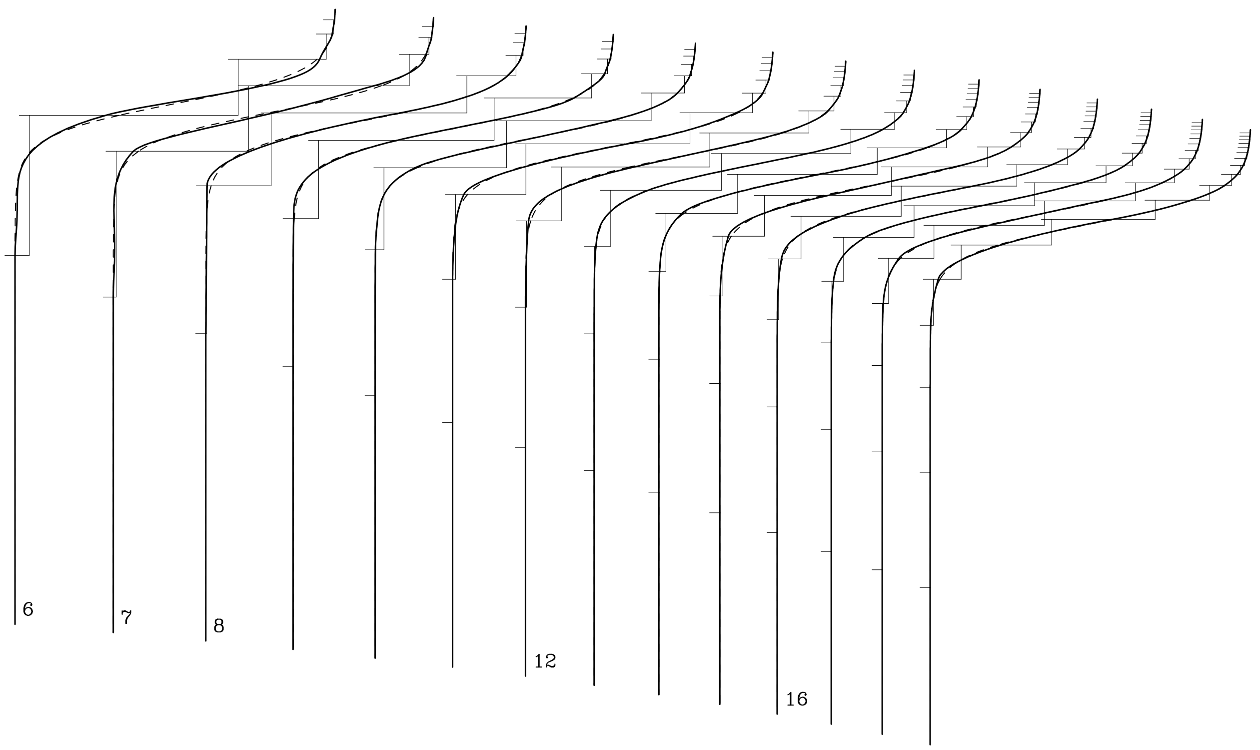

Figure 17. Profiles reconstructed by WENO (same as in Fig. 10), but with subsequent slope reconciliation step using power law function. The mild oscillations inside grid box with $k = 2$ on the leftmost profile are due to the approximation of power-law fit as a quartic polynomial.

that expression with square root in r.h.s. of (4.122) approaches 1 and if $\omega = 4/5$ in (4.90), these two become equivalent. Therefore, the power-law reconciliation algorithm described here may be interpreted as an alternative limiting for parabolic slope reconciliation, it is expected to have asymptotic convergence similar to that of parabolic spline.

In principle power-law function can produce monotonic fit for any degree of nonsmoothness, but when the resultant interfacial values and derivatives (4.123)–(4.109) are used in (3.7) and (3.14) it is still assumed that the distribution is given by quartic polynomial. The comparison of power-law functions with corresponding quartic polynomial is shown in Fig. 15 . In all cases solid and dashed curves have the same values and derivatives at both ends and the same average. The quartic fit is exact when α=2 , 3 and 4. When $3 < \alpha < 4$ quartic fit becomes nonmonotonic and produces negative values, which are, however remarkably small (the largest in absolute value is -0.0001964 when $x = 0.084768$ and $\alpha = 3.5$). After $\alpha = 4$ the negative values disappear and reappear again when $\alpha = 7$. Between $4 < \alpha < 5.4494$ the fit is monotone, then looses monotonicity again. In the context of finite-volume computation of pressure gradient force, where we are interested only in double integration (3.8), the oscillations shown in Fig. 15 do not cause any numerical instability until the center of gravity of the shaded element goes beyond $x = 1/2$, at which point the error effectively acts as negative stratification. It happens first time when $\alpha = 12$, at which point the quartic fit becomes extremely inaccurate. If a parabolic segment $\rho = \xi^2$, $0 < \xi < 1$ is replaced with $\rho = A\xi^\alpha$, with A chosen to retain the averaged value, then $A = (\alpha + 1)/3$ and the first derivative at $\xi = 1$ becomes $\alpha(\alpha + 1)/3$, Therefore we restricted $d_k + \frac{1}{2}$ to be no larger than $\alpha(\alpha + 1)$ of $(\overline{\rho}_k - \rho_{k-\frac{1}{2}})/H_k$ or $(\rho_{k+\frac{3}{2}} - \overline{\rho}_{k+1})/H_{k+1}$ depending which one belong to the grid box where variation increases due to correction to $\rho_{k+\frac{1}{2}}$. For all computations presented here we restricted $\alpha \leq 7$, which explains the appearance of factor of $\alpha(\alpha + 1) = 56$ in (4.111) and (4.114).

To save computational cost we replace (4.122), with its Padè rational function fit,

$$A = \frac{1}{5} B \cdot \frac{C\left(C + \frac{2}{55}|B|\right)}{C^2 + \frac{21}{275}|B|\left(C + \frac{1}{231}|B|\right)} \qquad (4.124)$$

which has no square root and only one division. This substitution produces virtually undistinguishable results for all values of ratio B/C within the range of interest,

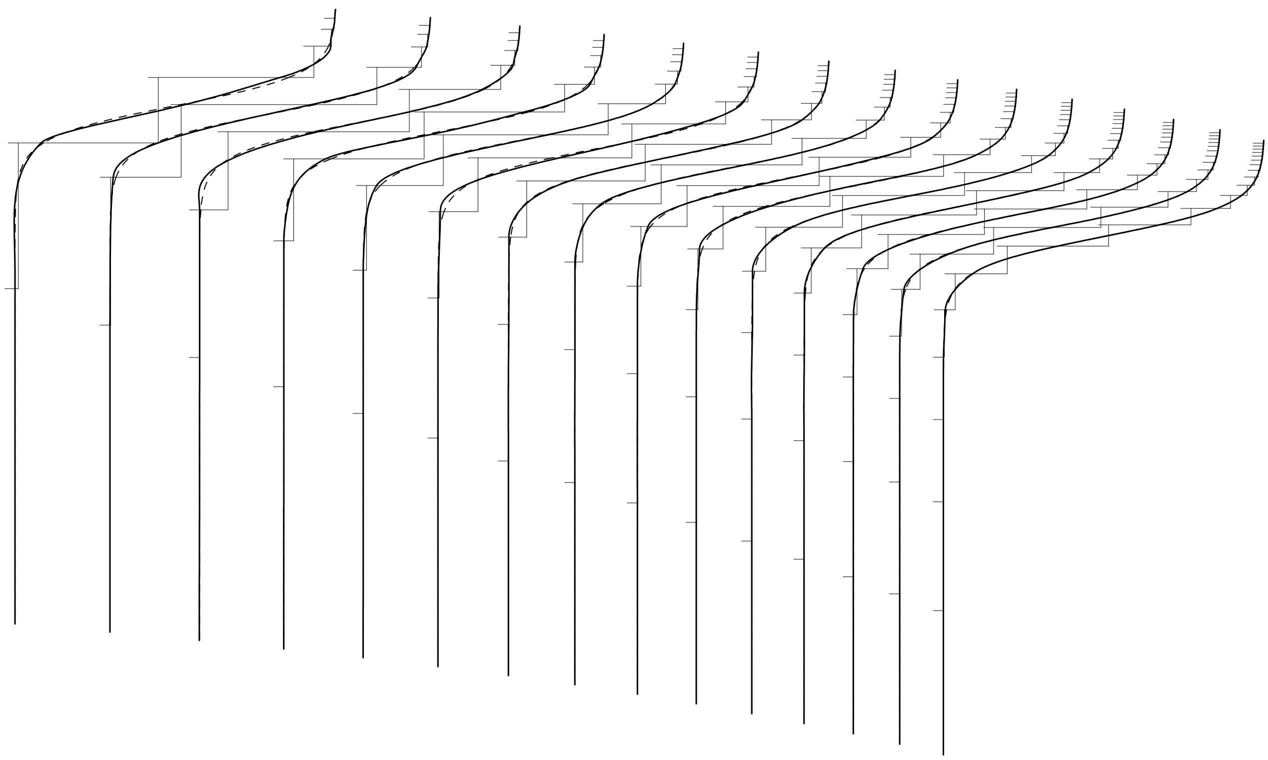

Figure 19. Vertical profiles reconstructed by quartic soline preconditioned by pseudo-quartic reconciliation algorithm.

[Equivalently to (4.127)–(4.128) this modification can be done by multiplying matrix $\mathbf{B}'_{k+\frac{1}{2}}$ in (4.43) by $\omega_{k+\frac{1}{2}}$ and adding term $(1-\omega_{k+\frac{1}{2}})\mathbf{d}^{(0)}_{k+\frac{1}{2}}$ into (4.42), while leaving (4.41) unchanged.]

The weighting function $\omega_{k+\frac{1}{2}}$ is set from the ratio of variations of interfacial values reconstructed by the preconditioning algorithm,

$$\omega_{k+\frac{1}{2}} = f_{k+\frac{1}{2}}\left(2 - f_{k+\frac{1}{2}}\right), \tag{4.129}$$

$$\omega_{k+\frac{1}{2}} = \left[f_{k+\frac{1}{2}}\left(3 - 3f_{k+\frac{1}{2}} + f^2_{k+\frac{1}{2}}\right)\right]^2, \tag{4.130}$$

$$\text{where} \quad f_{k+\frac{1}{2}} = \frac{v_k v_{k+1} + |v_k v_{k+1}|}{v_k^2 + v_{k+1}^2 + \epsilon}, \tag{4.131}$$

$$\text{where in its turn,} \quad \begin{aligned} v_k &= \rho^{(0)}_{k+\frac{1}{2}} - \rho^{(0)}_{k-\frac{1}{2}} \\ v_{k+1} &= \rho^{(0)}_{k+\frac{3}{2}} - \rho^{(0)}_{k+\frac{1}{2}} \end{aligned}$$

and ϵ is a small number (on computer roundoff precision level) just to avoid division by zero if $v_k = v_{k+1} = 0$. It should be recalled that if $r = v_k/v_{k+1}$, then

$$f_{k+\frac{1}{2}} = \frac{r + |r|}{1 + r^2} \tag{4.132}$$

which is commonly known as van Leer limiter. The possible weighting functions are plotted in Fig. 18 . The algorithm works with all three versions, (4.131), (4.129) or (4.130), with the later one resulting in slightly better performance.

Series of profiles reconstructed by the preconditioned quartic spline are shown in Fig. 19 . Unlike the basic quartic spline, the new algorithm does not produce spurious oscillations, producing results similar to the preconditioning algorithm, cf. Fig. 11 . In fact, there is no visual advantage of profiles in Fig. 19 in comparison with 11 , which is due to the fact that resolution on both of them is relatively coarse. A more detailed assessment (see next subsection) reveals that the preconditioned spline has quartic convergence rate for higher resolutions, which is far superior to Weighted ENO or Parabolic Reconciliation, which are used for preconditioning.

4.9. Accuracy and Convergence rate

After the reconstructed interpolants $\mathcal{P}_k(z')$ are known inside all grid boxes H_k, $k = 1, \dots, N$, the error measure (4.1) becomes

$$\epsilon = \sqrt{\frac{1}{h}\sum_{k=1}^{N}\int_{-H_k/2}^{+H_k/2}\left[\mathcal{P}_k(z') - \rho_{\text{exact}}(z')\right]^2 \mathrm{d}z'}\,, \tag{4.133}$$

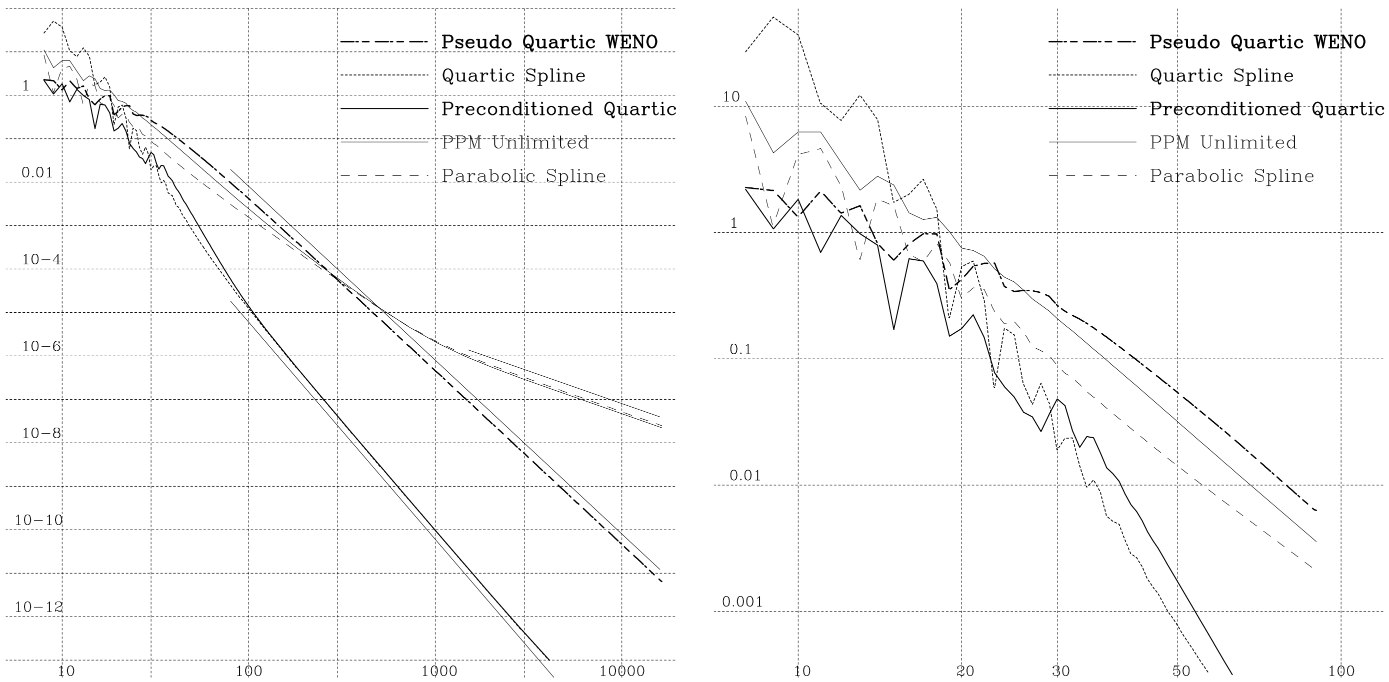

Figure 21. Quadratic error measure (vertical axis) as function of resolution (horizontal axis). **Left panel:** Comparison of convergence rates over the wide range of resolutions. Straight lines (starting from above) correspond asympthotic orders of N^{-2}, N^{-4} and N^{-5}. **Right panel:** An enlarged portion of left pannel corresponding to the coarse resolution part.

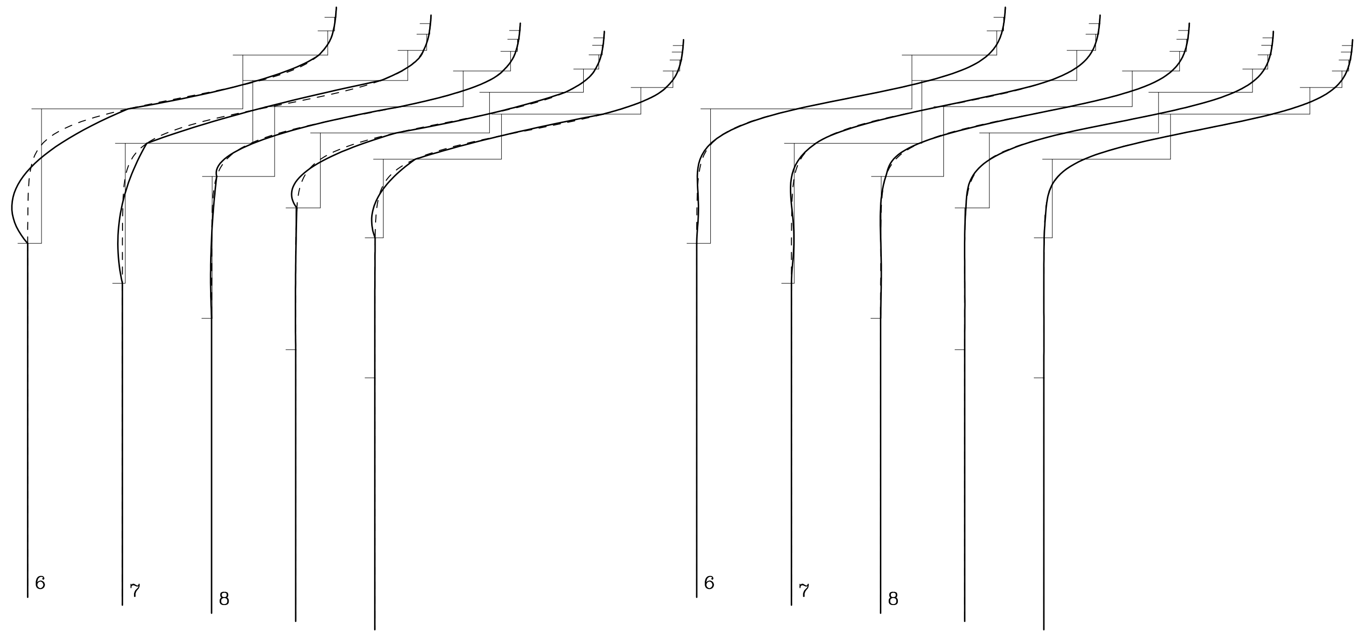

Figure 22. Coarse-resolution profiles obtained by parabolic (on the left) and quartic (on the right) polynomial fits based on *exact* interfacial values (both) and derivatives (quartic only). At this vertical resolutions $N = 6, 7, 8, 9, 10$ error of the parabolic fit is comparable with that of limited reconciliation algorithm, Fig. 11 , which suggests that with an appropriate reconstruction method errors of type (i) and (ii) are comparable. In the case of quartic fit error is always dominated by the error of interfacial values.

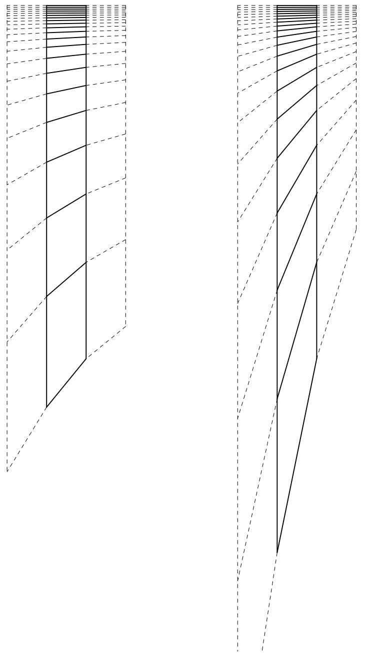

Figure 23. Two vertical grids used in hydrostatic balance experiments for $N = 20$.

practically relevant range of resolutions, for reasonable resolved density field, the actual error of reconstruction can not be simply estimated by a Taylor series analysis, which makes the notion of order of accuracy practically irrelevant.

It is also manifests that usage of high order accurate algorithms (such as quartic spline) without preconditioning or another monotonicity constraining algorithm is highly dangerous, which is, in fact, consistent with the general experience that although high-order methods may produce excellent results in idealized problems, they are practically useless for any real life application, cf. see Haidvogel & Beckmann, 1999 for a review. Nevertheless, high order methods can be successfully used in combination with monotonicity constraints.

5. Accuracy of Hydrostatic Balance

To access hydrostatic consistency error we setup bottom topography,

$$h_{\xi,\eta} = h_0 + \Delta x \cdot [Grad_\xi \cdot \xi + Grad_\eta \cdot \eta] \qquad (5.1)$$

where ξ, η are nondimensional horizontal coordinates (basically ξ and η are both incremented by 1 between grid points); $h_0 = -4875$ is median depth; $Grad_\xi = 400$, $Grad_\eta = 1600$ are topographic slopes and Δx is parameter to control refinement.

For a chosen number of vertical grid boxes N, Δx may be chosen according to one of the three algorithms:

$$\begin{array}{ll} \Delta x = 20/N & \text{proportional refinement} \\ \Delta x \equiv 1 & \text{vertical refinement only} \\ \Delta x = \sqrt{20/N} & \text{“semi-proportional” refinement} \end{array} \qquad (5.2)$$

so, for example, if $N = 20$ (hence $\Delta x = 1$), then ξ component of pressure gradient force is computed between two points with $h_{i-1,j} = -4275$ and $h_{i,j} = -3875$ respectively, while η component between $h_{i,j-1} = -5475$ and $h_{i,j} = -3875$. This choice corresponds to "r-factors" (cf., Beckmann & Haidvogel, 1993) of 0.05 in ξ-direction, which considered "moderate", and 0.2 in η-direction, which is "steep".

Once Δx is chosen and $h_{\xi,\eta}$ is known, then vertical grid is generated by (4.14) with parameters $\theta = 7$ and $h_c = 200$ specified there. After that, density profile is set by Eq. (4.15) with all parameters specified there (this is the same tanh-profile which is used to test reconstruction algorithms). Although for the base resolution of $N = 20$ and specified vertical stretching algorithm (4.14), in both cases grids are hydrostatically consistent in sense that $r \leq 1$ in each grid box (where r is defined by Eq. (3.25)), see Fig. 23 , this condition will be violated in the case of non-proportional refinement.

Since in all these experiments density is assumed to be a function of depth, all pressure gradient forces computed here are considered as spurious.

Once the finite-volume pressure gradient force $PGF_{i+\frac{1}{2},k}$ is computed at each grid box $\Delta\mathcal{V}_{i+\frac{1}{2},k}$ throughout vertical column $k = 1, \ldots N$, the quadratic error measure is defined as,

$$\epsilon = \sqrt{\sum_{k=1}^{N} \left(PX_{i+\frac{1}{2},k}\right)^2 \cdot \Delta\mathcal{V}_{i+\frac{1}{2},k} \Big/ \sum_{k=1}^{N} \Delta\mathcal{V}_{i+\frac{1}{2},k}} \qquad (5.3)$$

where

$$PX_{i+\frac{1}{2},k} = PGF_{i+\frac{1}{2},k} / \Delta\mathcal{V}_{i+\frac{1}{2},k} \qquad (5.4)$$

and

$$\Delta\mathcal{V}_{i+\frac{1}{2},k} = \frac{1}{2}\left(z_{i+1,k+\frac{1}{2}} - z_{i+1,k-\frac{1}{2}} + \right. \qquad (5.5)$$
$$\left. + z_{i,k+\frac{1}{2}} - z_{i,k-\frac{1}{2}}\right) .$$

Occasionally we interested in contribution of baroclinic pressure gradient into barotropic mode, which is judged by its own error measure,

$$\epsilon_{\text{bar}} = \sum_{k=1}^{N} PGF_{i+\frac{1}{2},k} \Big/ \sum_{k=1}^{N} \Delta\mathcal{V}_{i+\frac{1}{2},k} . \qquad (5.6)$$

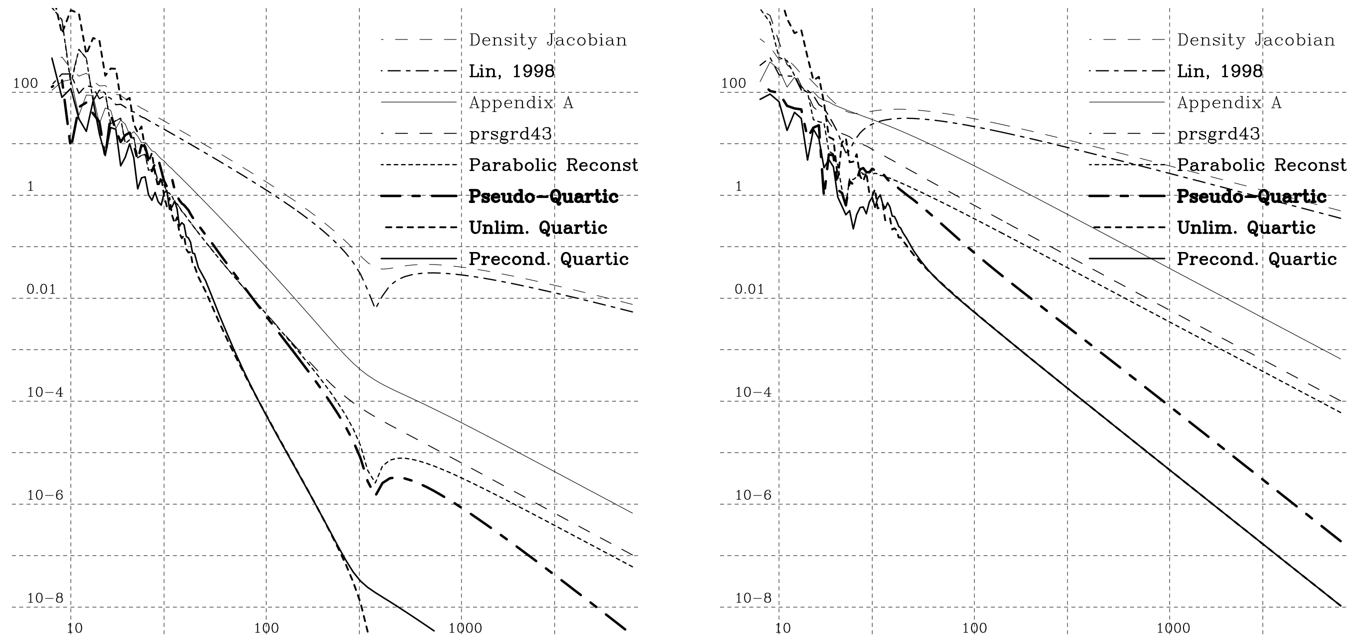

Figure 25. Same as Fig. 24 , expect for "semi-proportional" refinement

Convergence of pressure gradient error in terms of ϵ for various methods is shown in Fig. 24 , 25 for a wide range of vertical resolutions. Standard density Jacobian and Lin's methods exhibit second order convergence in the case of proportional refinement. Since these two are the most widely used, their performance provides a benchmark when evaluating all other methods. Methods based on parabolic fits for density field as well as scheme derived in Appendix A show asymptotic convergence consistent with fourth order of accuracy. Quartic schemes have sixth order asymptotic rate.

In the case of $\Delta x = \text{const}$ convergence stops after vertical refinement reaches certain limit. This behavior is expected, Haney, 1991. The residual error can be viewed as measure of tolerance of different PGF schemes to hydrostatically inconsistent grids (in sense $r > 1$, see Eq. (3.25)). This is an important measure, since our primary goal is to design methods which retain as much accuracy as possible in such conditions.

Comparison of left and right top panels of Fig. 24 shows that error actually *decreases* for most of the schemes when going from moderate to steep topography, especially for vertical resolutions within the range $N = 10$ to 30. This effect is explained by partial error cancellation of Jacobian schemes when aspect ratio parameter r passes 1 in the region of maximum vertical gradient (even thought grids on the left are "hydrostatically consistent" (in sense of Haney, 1991) and grids on the right are "inconsistent" in the lowest portion, at the place when density changes most $r \leq 1$ and r is close to 1 for the grids on the right. This effect also explains the local *minumum* of error on the left and right lower panels of Fig. 24 for $N \approx 76$ and $N \approx 22$ respectively, as well as on left and right panels of Fig. 25 for $N \approx 23$ and $N \approx 394$. In fact in all these minima correspond to the condition when density-stratification-weighted grid aspect ratio

$$r_\rho = \sum_{k=1}^{N} r_{i+\frac{1}{2},k} \cdot \Delta\rho_{i+\frac{1}{2},k} \Bigg/ \sum_{k=1}^{N} \Delta\rho_{i+\frac{1}{2},k} \,, \tag{5.7}$$

where $r_{i+\frac{1}{2},k}$ is defined by (3.25) and

$$\Delta\rho_{i+\frac{1}{2},k} = \frac{1}{2} \cdot \Big(\rho_{i+1,k+\frac{1}{2}} - \rho_{i+1,k-\frac{1}{2}} + \\ + \rho_{i,k+\frac{1}{2}} - \rho_{i,k-\frac{1}{2}} \Big) \tag{5.8}$$

crosses threshold of 1. In the case of propotional refinement this ratio is kept approximately constant and and equal to 0.23 and 0.92 for moderate and steep cases respectively.

In the case of $\Delta x = \text{const}$ refinement the asymptotic limit of hydrostatic error demonstrated the advantage of quartic and pseudo-quartic methods over parabolic and liner, both in terms of value of error as well as ability of the scheme to remain accurate on hydrostatically inconsistent grids. This is clearly seen on the bottom right panel of Fig. 24, when, after passing $r_\rho \approx 1$ at $N = 22$, error of Lin's method starts increasing, while error of quartic scheme continues to decrease and asymptotes to the limit two order of magnitude smaller than that of Lin. Comparison of the asymptotic limits between left and right lower panels of Fig. 24 for quartic algorithms shows difference of slightly less that 4 orders of magnitude, which in consistent with sixth order convergence, given that the differences $z_{i+1,k+\frac{1}{2}} - z_{i,k+\frac{1}{2}}$ are 4 times greater for the right panel and $4^6 = 4096$.

Another observation to be made is the fact that algorithm from Appendix A shows the the most significant degradation of accuracy when going from moderate to steep topography: on the lower left panel of Fig. 24 its asymptotic level of error is comparable with the other parabolic scheme and significantly better that that of Lin's. On the right panel it almost loses its advantage over Lin's method. Similar tendencies are observed on all other panels.

This phenomenon is explained by the fact that in method derived in Appendix A approximation of pressure distribution along the top facets of grid boxes is done using extra points in horizontal directions, rather that projecting vertical derivatives of density field assuming non-orthogonal grid in a manner of Eq. (3.9). In the case of steep topography and/or non-proportional refinement, when the differences $z_{i+1,k+\frac{1}{2}} - z_{i,k+\frac{1}{2}}$ do not decrease or decrease at slower rate than corresponding vertical differences, the error hydrostatic balance is dominated by it. Method based on projection (3.9) are free of this limitation.

Fig. 26 shows coarse resolution portion of Fig. 24. Comparison with Fig. 21 indicates that at coarse resolution error in pressure gradient force is dominated by the error in density reconstruction. Clearly, the use of unlimited quartic and unlimited parabolic splines results in the worst coarse resolution errors exceeding that of Lin's method, however pseudo-quartic polynomial fit and preconditioned quartic spline provide robust and accurate behavior.

Perhaps the most striking conclusion one can draw from Fig. 26 is the fact that in this practically useful range of vertical resolutions the error *can not* be judged from the order of accuracy of scheme based on analysis of Taylor series. Although not the most accurate in general, standard density Jacobian and Lin's method provide robust coarse resolution behavior. Any attempt to their improve accuracy in this limit by using nonconstrained high-order methods is doomed to failure.

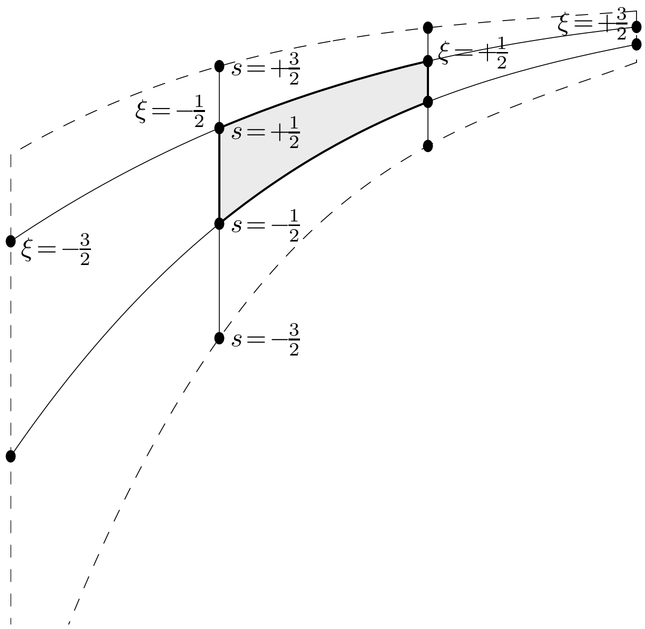

Figure 27. Computational stencil for pressure gradient scheme based on direction-independent, Lagrangian cubic fit. The shaded element repesents the $u_{i+\frac{1}{2},k}$. Bullets indicate pressure points which are involved in computation. Labels $s = +\frac{1}{2}$, etc indicate values of fractional coordinates at the nearest pressure point. Because cubic interpolation is used to reconstruct coordinate lines, this Fig. appears to be a smooth version of Fig. 1.

Appendix A1: A Pressure-Jacobian Scheme Using Direction-independent Lagrangian Cubic Fits

Lets assume that the $P_{i,k+\frac{1}{2}}$ is known at the vertices of grid box $z_{i,k+\frac{1}{2}}$ at every i and k. We introduce a local fractional coordinate s, such that it runs along a side facet of grid box, so that $s = \pm\frac{1}{2}$ at the vertices $z_{i,k\pm\frac{1}{2}}$, see Fig. 28, so that

$$FX_{i,k} = \int_{z_{i,k-\frac{1}{2}}}^{z_{i,k+\frac{1}{2}}} P(z')\,\mathrm{d}z' = \int_{-\frac{1}{2}}^{+\frac{1}{2}} P(s)\frac{\partial z}{\partial s}(s)\mathrm{d}s\,. \quad \text{(A1.1)}$$

Similarly, let ξ be a local fractional coordinate running along the top facet of the grid box, so that

$$FC_{i+\frac{1}{2},k+\frac{1}{2}} = \int_{z_{i+1,k+\frac{1}{2}}}^{z_{i,k+\frac{1}{2}}} P(z')\,\mathrm{d}z' = \int_{-\frac{1}{2}}^{+\frac{1}{2}} P(\xi)\frac{\partial z}{\partial \xi}(\xi)\mathrm{d}\xi\,. \text{(A1.2)}$$

$$-\frac{1}{12}\left\{\left(P_{i,N+\frac{1}{2}}-2P_{i,N-\frac{1}{2}}+P_{i,N-\frac{3}{2}}\right)\times\right.\qquad\text{(A1.13)}$$
$$\times\left(z_{i,N+\frac{1}{2}}-z_{i,N-\frac{1}{2}}\right)$$
$$-\left(P_{i,N+\frac{1}{2}}-P_{i,N-\frac{1}{2}}\right)\times$$
$$\left.\times\left(z_{i,N+\frac{1}{2}}-2z_{i,N-\frac{1}{2}}+z_{i,N-\frac{3}{2}}\right)\right\}$$

and

$$FX_{i,1}=\frac{1}{2}\left(P_{i,\frac{3}{2}}+P_{i,\frac{1}{2}}\right)\left(z_{i,\frac{3}{2}}-z_{i,\frac{1}{2}}\right)\qquad\text{(A1.14)}$$
$$-\frac{1}{12}\left\{\left(P_{i,\frac{5}{2}}-2P_{i,\frac{3}{2}}+P_{i,\frac{1}{2}}\right)\left(z_{i,\frac{3}{2}}-z_{i,\frac{1}{2}}\right)\right.$$
$$\left.-\left(P_{i,\frac{3}{2}}-P_{i,\frac{1}{2}}\right)\left(z_{i,\frac{5}{2}}-2z_{i,\frac{3}{2}}+z_{i,\frac{1}{2}}\right)\right\}.$$

Since the first term in r.h.s. of (A1.10), (A1.11), (A1.13) and (A1.14) coincides with that of Lin's scheme (cf. (2.6) and (2.7)), the remaining terms (which are multiplied by 1/1440 and 1/12) can be considered as high-order correction to Lin's method.

By its construction, the algorithm described here has zero hydrostatic pressure gradient error if P and z are linear, quadratic or cubic polynomials of underlying coordinates ξ, s (i.e. in coordinates in σ-space). Because most commonly used coordinate stretching involve transcendental function, we do not expect pressure gradient error to vanish exactly if $P(z)=z$, z^2, z^3 and any combination thereof, except, of course, if the coordinate stretching is linear. This, however, cannot be considered as a disadvantage of the method derived here, because at the first place the use of nonlinear coordinate stretching is motivated by the desire to "absorb" some of the nonlinearity of physical fields, say refinement near the top, where stratification is the strongest. Therefore, in σ-space pressure field is generally expected to be a smoother function that that in physical space, so it can be better approximated using polynomial fit in σ- rather than in physical space. It is also implied that the underlying topography and the mapping function $z=z(\xi,s)$ are reasonably smooth on the grid scale, so it can be accurately represented by the polynomial fit.

It should be also noted, that the above algorithm can be also applied to construct a density-Jacobian scheme in a manner described in (1.7), however this scheme cannot be cast into finite-volume framework because the interpalation algorithms (A1.6) and (A1.12) interpret $f_{\pm\frac{1}{2}}$ and $f_{\pm\frac{3}{2}}$ as *exact* values at corresponding location rather than grid-box averages.

Appendix B: On the stability limits of defferred correction

For the sake of simplicity we only consider grid with uniform stiffness parameter r defined by Eq. (3.25). In this case substitution of (3.26) into (3.22) reduces to

$$PX^{(1)}=PX^{(0)}+\frac{r}{12}\cdot\Lambda[PX^{(0)}]\qquad\text{(B.1)}$$

where, in the case of $r>0$, $\Lambda[PX]$ is a discrete operator

$$\Lambda[PX]|_{i+\frac{1}{2},k}=-\frac{1}{2}PX_{i-\frac{1}{2},k+1}+\frac{1}{2}PX_{i+\frac{1}{2},k+1}$$
$$+\frac{1}{2}PX_{i-\frac{1}{2},k}-PX_{i+\frac{1}{2},k}+\frac{1}{2}PX_{i+\frac{3}{2},k}\qquad\text{(B.2)}$$
$$+\frac{1}{2}PX_{i+\frac{1}{2},k-1}-\frac{1}{2}PX_{i+\frac{3}{2},k-1},$$

which can be symbolically represented as

$$\Lambda=\begin{bmatrix}-{}^1/_2 & +{}^1/_2 & \\ +{}^1/_2 & -1 & +{}^1/_2 \\ & +{}^1/_2 & -{}^1/_2\end{bmatrix}.\qquad\text{(B.3)}$$

Eq. (B.1) can be viewed as the starting step of the iterative procedure,

$$PX^{(m)}=PX^{(0)}+\frac{r}{12}\cdot\Lambda[PX^{(m-1)}]\ ,m=1,2,...\qquad\text{(B.4)}$$

if this procedure converges, its limit $PX^{(\infty)}$ must satisfy

$$PX^{(\infty)}=PX^{(0)}+\frac{r}{12}\cdot\Lambda[PX^{(\infty)}].\qquad\text{(B.5)}$$

Subtraction of (B.5) from (B.4) yields

$$PX^{(m)}-PX^{(\infty)}=\frac{r}{12}\cdot\Lambda[PX^{(m-1)}-PX^{(\infty)}]\ ,\qquad\text{(B.6)}$$

or, simply

$$\delta PX^{(m)}=\frac{r}{12}\cdot\Lambda[\delta PX^{(m-1)}]\ ,\qquad\text{(B.7)}$$

which can be interpreted as equation for decay of perturbation of the solution from its "true limit" $PX^{(\infty)}$. The procedure (B.4) is stable and convergent if for all possible perturbation modes is (B.7) the amplification factor is less than 1.

Now we consider perturbations in form of Fourier component,

$$\delta PX_{i,k}=\mathrm{e}^{\mathrm{i}k_x\Delta xi+\mathrm{i}k_z\Delta zk}\qquad\text{(B.8)}$$

where $-\pi\le k_x\Delta x\le+\pi$ and $-\pi\le k_z\Delta z\le+\pi$. Obviously

$$\Lambda[\delta PX]=\lambda\cdot\delta PX\,,\qquad\text{(B.9)}$$

is bounded away from zero for any ξ. Straightforward resolution of (C.11)–(C.12) yeilds

$$\tilde{\rho}_k = \hat{\rho}_k \cdot \frac{\frac{\sin\xi}{\xi}\left(\frac{5}{6}+\frac{1}{6}\cos\xi\right)}{\frac{11}{20}+\frac{13}{30}\cos\xi+\frac{1}{60}\cos(2\xi)} \approx \tag{C.15}$$
$$\approx \hat{\rho}_k\left(1-\frac{1}{7}\cdot\frac{\xi^6}{720}+...\right)$$

$$\hat{d}_k = ik\hat{\rho}_k \cdot \frac{\frac{1}{\xi^2}\left(1-\frac{2}{3}\cos\xi-\frac{1}{3}\cos(2\xi)\right)}{\frac{11}{20}+\frac{13}{30}\cos\xi+\frac{1}{60}\cos(2\xi)} \approx \tag{C.16}$$
$$\approx ik\hat{\rho}_k\left(1+\frac{1}{30}\cdot\frac{\xi^4}{24}+...\right),$$

which indicates the sixth order of accuracy for the interpolated value and the fourth order for the derivative, since ideally $\tilde{\rho}_k$ should be equal to $\hat{\rho}_k$ and $\hat{d}_k$ should be the same as $ik\hat{\rho}_k$.

Therefore, is convenient to introduce spectral amplitudes $\mathcal{A}(k)$ and $\mathcal{K}(k)$, so that (C.15)—(C.16) and also (C.10) may be rewritten as

$$\tilde{\rho}_k = \mathcal{A}(k)\cdot\hat{\rho}_k \tag{C.17}$$
$$\hat{d}_k = i\mathcal{K}(k)\cdot\hat{\rho}_k\,, \tag{C.18}$$

which are then compared with their exact values of 1 and k as well as with similar characteristics of other methods.

Comparison against spectral amplitudes corresponding to the local polynomial fits of second-, fourth- and sixth-orders,

$$\tilde{\rho}_k = \hat{\rho}_k \cdot \frac{\sin\xi}{\xi} \tag{C.19}$$
$$\tilde{\rho}_k = \hat{\rho}_k \cdot \frac{\sin(\xi/2)}{\xi/2}\cdot\left(\frac{7}{6}\cos\frac{\xi}{2}-\frac{1}{6}\cos\frac{3\xi}{2}\right) \tag{C.20}$$
$$\tilde{\rho}_k = \hat{\rho}_k \cdot \frac{\sin(\xi/2)}{\xi/2}\cdot\left(\frac{37}{30}\cos\frac{\xi}{2}- \right. \tag{C.21}$$
$$\left. -\frac{4}{15}\cos\frac{3\xi}{2}+\frac{1}{30}\cos\frac{5\xi}{2}\right)$$

as well as parabolic spline (C.10), indicates significant gain in accuracy in term of spectral bandwidth, Fig. 29. For example, the accuracy of reproduction of the Fourier amplitude corresponding to $4\Delta x$ is about 1% for the quartic spline algorithm, while for all others presented in Fig. 29 it ranges from 5 to 30%.

Interfacial values for the first derivative for local polynomial fits are obtained by analytical differentiation of the polynomials. Their spectral amplitude for the second-, fourth-, and sixth-orders of accuracy are,

$$\hat{d}_k = ik\hat{\rho}_k \cdot \left(\frac{\sin(\xi/2)}{\xi/2}\right)^2 \tag{C.22}$$

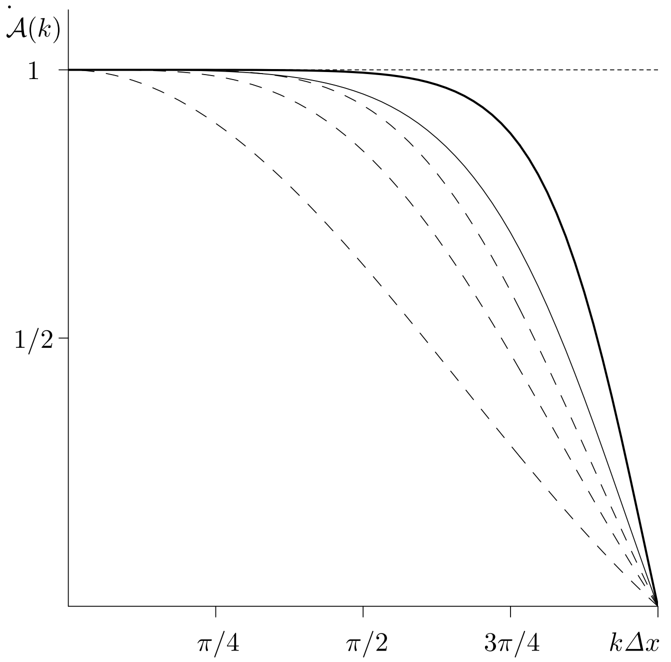

Figure 28. Spectral amplitudes of interfacial values obtained by different reconstruction algorithms. Dashed curves from below up correspond to local polynomial fits from second- to sixth orders of accuracy. Thin solid line — parabolic spline; bold solid line — quartic spline.

$$\hat{d}_k = ik\hat{\rho}_k \cdot \frac{\sin(\xi/2)}{(\xi/2)^2}\left(\frac{5}{4}\sin\frac{\xi}{2}-\frac{1}{12}\sin\frac{3\xi}{2}\right) \tag{C.23}$$
$$\hat{d}_k = ik\hat{\rho}_k \cdot \frac{\sin(\xi/2)}{(\xi/2)^2}\left(\frac{49}{36}\sin\frac{\xi}{2}- \right. \tag{C.24}$$
$$\left. -\frac{5}{36}\sin\frac{3\xi}{2}+\frac{1}{90}\sin\frac{5\xi}{2}\right),$$

which are shown in Fig. 29, as dashed curves. Comparison with (C.16) show that Fourier amplitude of derivative estimated by the quartic spline algorithm is generally closer to the ideal line $\mathcal{K}(k)=k$ than that for local polynomial fits of the same accuracy. It also shows that it lies above the ideal line, which is not unusual behaviour for compact differencing schemes, cf. Chu & Fan, 1997, Chu & Fan, 1998[12].

[12]It has to be emphasised, that despite obvious algorithmic similarities (e.g., 3-point stencil; tri-diagonal and block tri-diagonal systems) none of the algorithm in the present study actually coincides with that derived in there references. The difference lies in the fact that in the present study the gridded data is interpreted in volume-integrated sense (rather than interpreted as set of values at grid points) as well as in the fact that the design principle here is to achieve continuity of higher order derivatives eventually with emphasis on nonuniformly stretched grids (rather than achieving the highest possible order of accuracy for a given complexity of the algorithm).

Fourier image of (D.2) is then,

$$\tilde{\rho}_k^{(m+1)} = \frac{3}{2}\omega\hat{\rho}_k\frac{\sin\xi}{\xi} + \tilde{\rho}_k^{(m)}\left[1-\omega\left(1+\frac{\cos\xi}{2}\right)\right] \quad \text{(D.5)}$$

where we $\tilde{\rho}_k^{(m)}$ is Fourier amplitude of interfacial values $\rho_{j+\frac{1}{2}}$.

If one assumes that this procedure converges when $m \to \infty$, its limit may be found by substituting both $\tilde{\rho}_k^{(m+1)}$ and $\tilde{\rho}_k^{(m)}$ with $\tilde{\rho}_k^{(\infty)}$ in (D.5) and then solving it for $\tilde{\rho}_k^{(\infty)}$ directly,

$$\tilde{\rho}_k^{(\infty)} = \hat{\rho}_k\frac{\frac{3}{2}\frac{\sin\xi}{\xi}}{1+\frac{1}{2}\cos\xi} \quad \text{(D.6)}$$

which, indeed, coincides with (C.10). Now (D.5) may be rewritten in terms of deviation from the converged solution, $\tilde{\epsilon}_k^{(m)} \equiv \tilde{\rho}_k^{(m)} - \tilde{\rho}_k^{(\infty)}$,

$$\tilde{\epsilon}_k^{(m+1)} = \tilde{\epsilon}_k^{(m)}\cdot\left[1-\omega\left(1+\frac{1}{2}\cos\xi\right)\right], \quad \text{(D.7)}$$

from which we see that the choice of $\omega = 2/3$ corresponds to the case when error is reduced by two orders of accuracy during each iteration, since

$$1-\frac{2}{3}\left(1+\frac{1}{2}\cos\xi\right) \approx \frac{1}{3}\frac{\xi^2}{2!} + ... \quad \text{(D.8)}$$

Finally, it can be immediately verified that substitution of the initial value (D.1) into (D.2) results in

$$\rho_{j+\frac{1}{2}}^{(1)} = -\frac{1}{12}\overline{\rho}_{j-1} + \frac{7}{12}\overline{\rho}_j + \frac{7}{12}\overline{\rho}_{j+1} - \frac{1}{12}\overline{\rho}_{j+2} \quad \text{(D.9)}$$

which is nothing else but the conventional fourth-order approximation for the interfacial value on a uniform grid. Remarkably, if this $\rho^{(1)}$ is then substituted into (D.2) where we set $\omega = 4/5$, then

$$\rho_{j+\frac{1}{2}}^{(2)} = \frac{1}{60}\overline{\rho}_{j-2} - \frac{2}{15}\overline{\rho}_{j-1} + \frac{37}{60}\overline{\rho}_j + \frac{37}{60}\overline{\rho}_{j+1} - \frac{2}{15}\overline{\rho}_{j+2} + \frac{1}{60}\overline{\rho}_{j+3} \quad \text{(D.10)}$$

recovers the sixth-order interpolation scheme.

References

Arakawa, A., and M. J. Suarez, 1983, Vertical differencing of the primitive equations in sigma coordinates. *Monthly Weather Review*, **111**, 34-45.

Beckmann, A., and D. B. Haidvogel, 1993: Numerical simulation of flow around a tall isolated seamount. Part. 1: Problem formulation and model accuracy. *Journ. Phys. Ocean.*, **23**, 1736-1753.

Beckmann, A., and D. B. Haidvogel, 1997: A numerical simulation of flow at Fieberling Guyot. *Journ. Geophys. Res.*, **102**, 5595-5613.

Blumberg, A. F. and G. L. Mellor, 1987: A description of a three-dimensional coastal ocean circulation model. In *Three-dimensional Coastal Ocean Models*, ed. N. Heaps (Pub. AGU), pp. 1-16.

Chu, P. C. and C. Fan, 1997: Sixth-order difference scheme for sigma coordinate ocean models. *Journ. Phys. Ocean.*, **27**, 2064-2071.

Chu, P. C. and C. Fan, 1998: A three-point combined compact difference scheme. *Journ. Comp. Phys.*, **140**, 370-399.

Colella, P. and P. R. Woodward, 1984: The Piecewise Parabolic Method (PPM) for gas dynamical simulations. *Journ. Comp. Phys.*, **54**, 174-201.

Gary, J. M., 1973: Estimate of truncation error in transformed coordinate primitive equation atmospheric models. *Journ. Atmosph. Sci.*, **30**, 223-233.

Gradshteyn, I. S., and I. M. Ryzhik, Table of Integrals, Series and Products. Academic Press, 1965, 1086 pages.

Haidvogel, D. B., A. Beckmann, D. C. Chapman, and R.-Q. Lin, 1993: Numerical simulation of flow around a tall isolated seamount: Part II: Resonant generation of trapped waves. *Journ. Phys. Ocean.*, **23**, 2373-3291.

Haidvogel, D. B., and A. Beckmann, 1999: Numerical Ocean Modeling. *Imperical College Press.*, London, 330 pages.

Harten, A., B. Engquist, S. Osher, and S. Chakravarty, 1987: Uniformly high-order accurate essentially non-oscillatory schemes III. *Journ. Comp. Phys.*, **71**, 231-303.

Haney, R. L., 1991: On the pressure gradient force over steep topography in sigma coordinate ocean models. *Journ. Phys. Ocean.*, **21**, 610-618.

Jackett, D. R. and T. J. McDougall, 1995: Minimal Adjustment of Hydrostatic Profiles to Achieve Static Stability. *Journ. Atmos. Oceanic Technology*, **12**, 381-389.

This preprint was prepared with the AGU LaTeX macros v3.1.
File pgf1 formatted 2003 July 15.